9-1-2018

Evaluation and Quantification of Diffractive Plenoptic Camera Algorithm Performance

Jack A. Shepherd III

EVALUATION AND QUANTIFICATION OF DIFFRACTIVE PLENOPTIC CAMERA ALGORITHM PERFORMANCE

DISSERTATION

Jack A. Shepherd III, Captain, USAF

AFIT-ENP-DS-18-S-026

DEPARTMENT OF THE AIR FORCE
AIR UNIVERSITY

AIR FORCE INSTITUTE OF TECHNOLOGY

Wright-Patterson Air Force Base, Ohio

AFIT-ENP-DS-18-S-026

EVALUATION AND QUANTIFICATION OF DIFFRACTIVE PLENOPTIC CAMERA ALGORITHM PERFORMANCE

DISSERTATION

Presented to the Faculty

Department of Aeronautics and Astronautics

Graduate School of Engineering and Management

Air Force Institute of Technology

Air University

Air Education and Training Command

In Partial Fulfillment of the Requirements for the

Degree of Doctorate of Philosophy in Applied Physics

Jack A. Shepherd III, B.S., M.A.T., M.S.

Captain, USAF

August 2018

DISTRIBUTION STATEMENT A.
APPROVED FOR PUBLIC RELEASE; DISTRIBUTION UNLIMITED.

AFIT-ENP-DS-18-S-026

EVALUATION AND QUANTIFICATION OF DIFFRACTIVE PLENOPTIC CAMERA ALGORITHM PERFORMANCE

Jack A. Shepherd III, B.S., M.A.T, M.S.

Captain, USAF

Committee Membership:

Lt. Col. Anthony L. Franz, PhD
Dissertation Advisor

Dr. Michael A. Marciniak
Committee Member

Dr. Michael Hawks
Committee Member

Dr. Benjamin Akers
Committee Member

Abstract

A diffractive plenoptic camera is a novel approach to the traditional plenoptic camera which replaces the main optic with a Fresnel zone plate making the camera sensitive to wavelength instead of range. However, algorithms are necessary to reconstruct the image produced by plenoptic cameras. While many algorithms exist for traditional plenoptic cameras, their ability to create spectral images in a diffractive plenoptic camera is unknown. This paper evaluates digital refocusing, super resolution, and 3D deconvolution through a Richardson-Lucy algorithm as well as a new Gaussian smoothing algorithm. All of the algorithms worked well near the Fresnel zone plate design wavelength, but Gaussian smoothing provided better looking images at a cost of high computation time. For wavelengths off the design wavelength, 3D deconvolution produced the best images but also required more computation time. 3D deconvolution also had the best spectral resolution, which increased away from the design wavelength. These results, along with consideration of mission constraints and spectral content in the scene, can guide algorithm selection for future sensor designs.

Acknowledgments

I would like to express my sincere appreciation to my faculty advisor, Lt Col Anthony Franz, for his guidance and support throughout the course of this dissertation effort. The insight and experience was certainly appreciated. I would, also, like to thank my wife and new child for supporting me and putting up with the long hours necessary for me to complete this endeavor.

Jack A. Shepherd III

Table of Contents

List of Figures

Page

List of Tables

Page

EVALUATION AND QUANTIFICATION OF DIFFRACTIVE PLENOPTIC CAMERA ALGORITHM PERFORMANCE

I. Introduction

Future observational and DoD systems continue to head towards more compact designs. This can be seen in the advent of several new systems that have driven research in key areas. Some examples of this are satellites that have continuously decreased in size since the cost to enter orbit is directly proportional to the satellite's size and weight and are now dominated by cubesats that are completely contained in dimensions no bigger than 10 cm x 10 cm x 33 cm and weighing less than 5 kg [1]. Additionally, micro-UAVs are becoming extremely common in both military and civilian applications as cheaper and safer alternatives to larger aircraft, however, these too are very limited in both the size and weight of their payload [2]. This push towards small vehicles used for observations put an effective limit on the number of pieces of equipment that can be carried and, in general, will be limited to a single device [1].

Since space is so important for many of the current and future platforms, being able to collect a multitude of information from a single instrument is paramount. Recently, FalconSAT-7 was designed and built to prove this concept. It utilizes diffractive optics, specifically a photon sieve, in order to sample the underlying Fresnel zone pattern with pin holes [3]. This setup allows an optic that is larger than the cubesat it is contained within while also providing weight savings. Afterwards, it was suggested that a plentoptic camera system with a Fresnel zone plate (FZP) as the main optic could be used to conduct spectral imaging [4] and was demonstrated [5]. This allows both

imaging of the target as well as collecting spectral characterization with a single device. Utilizing a FZP in our plenoptic camera has allowed us to gain detail in the wavelength domain in place of the traditional depth information in a standard plenoptic camera. This work was also presented at the SPIE Defense and Commercial Sensing conference in 2018 [6].

Plenoptic systems do not produce a usable raw image. They require an algorithm to process the data from the plenoptic system in order to get an image [7]. There are many algorithms currently being used to process the plenoptic data to get the image [7] [8] [9] [10] [11]. Which of the many algorithms that can be used for the traditional plenoptic camera should we use in order to gain spectral information? Which of the algorithms produce the best results and where do each of the algorithms shine?

This dissertation describes the analysis of the plenoptic camera with Fresnel zone plate (FZP) imaging system in MATLAB in order to compare processing algorithm approaches for different desired capabilities. The second chapter provides a brief overview and description of the Fresnel zone plate, plenoptic cameras, and the combination of both. The third chapter provides a description of the processing algorithms used in the diffractive plenoptic camera. The fourth chapter provides an examination of the results the diffractive plenoptic camera. First, the results of a simulated single wavelength chart are examined. Then noise is added in order to ensure that the algorithms still function as expected under high noise conditions. Next, point sources are simulated in order to more clearly see how varying the wavelength separation from the FZP's design affects the efficacy of each of the algorithms. Then grayscale and more complicated images are examined in order to ensure that all algorithms maintain the

correct relative energies based on location and source brightness. Next, we examine several hyperspectral cases in order to judge the performance of the algorithms under conditions where the source is not monochromatic. Finally, the overall performance of the algorithms are examined based on the spatial range, spatial resolution, spectral range, spectral resolution, and required computation time.

II. Background

Chapter Overview

In this chapter, some of the background information necessary for understanding the research that was done will be reviewed. First, the traditional plenoptic cameras are discussed, including a brief introduction of their origin and how they work. Then Fresnel zone plates are described and some of the math necessary to get the design parameters is presented. Finally, the replacement of the main optic in a traditional plenoptic camera with a Fresnel zone plate is discussed.

Plenoptics

A plenoptic camera, sometimes called a light-field camera in reference to both the position and angle of the light rays within the camera, utilizes a primary optic and a detector array, as in a traditional camera. However, an array of micro-lenses is placed between the primary optic and the detector array at the focal point of the primary optic. The basic geometry of this setup can be seen in Figure 1. The original idea of a light-field camera is extremely old. In 1908, Lippmann proposed what he called “integral photography” in which he was able to produce crude integral photographs by using a plastic sheet that he embossed with an array of artificial micro-lenses. These micro-lenses were made by inserting small glass beads closely together into a random pattern onto the surface of the photographic emulsion [12]. Adelson and Bergen were the first from the modern era to propose the concept of plenoptics in 1991 [13]. The very next year, Adelson and Wang suggested a special camera to utilize this concept and outlined

the idea of a plenoptic camera that closely mimicked Lippmann's original work back in 1908 except with more modern and updated equipment [14] and Ng built one as well more recently [11].

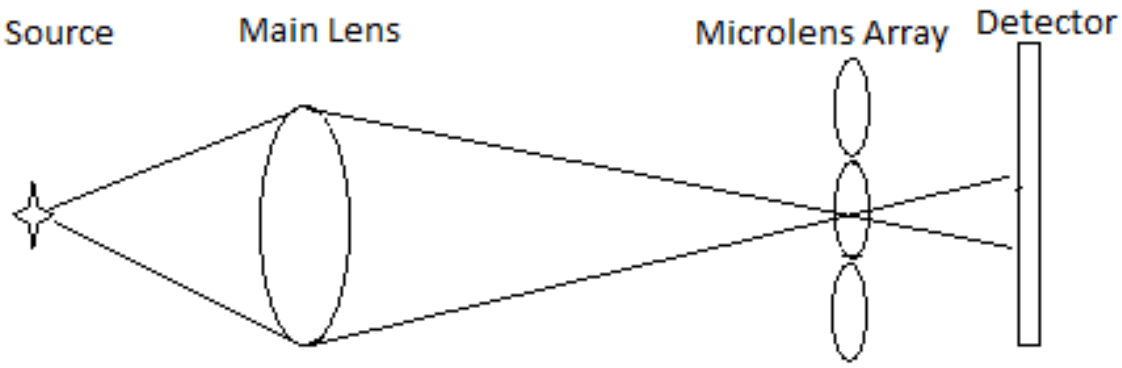

Figure 1. A drawing of a plenoptic camera utilizing a large main lens along with a smaller micro-lens array imaging onto a detector.

With this setup, each micro-lens collects every angle of rays from each distinct point within the camera system from each point on the main lens [7] [11]. This means that the plenoptic camera trades spatial resolution for that angular information. The angular sampling of the light field is set by the size of the pixels in the detector. The level of the spatial sampling is set by the size of the micro-lenses. This light field can be tracked by mapping each light ray as it passes through the primary optic and then following it until it crosses the micro-lens array. Thus, the full range of values corresponding to all projected light rays correspond to the smaller range of the collected rays on the micro-lenses. Then, we can represent the radiance of a plenoptic function with separate positional dimensions and angular dimensions [5].

Within the plenoptic camera, the full range of angles from a single point is recorded behind each micro-lens in the micro-lens array [11]. This means that the spatial resolution is determined by the size of the micro-lenses and the angular resolution is determined by the size of the pixels on the detector. It also means that the same pixel behind each micro-lens corresponds to the different points from the main lens travelling at a different angle. Using this information, these micro-lens images can be combined in order to form what are commonly called sub-aperture images [11]. These are formed by combining the same pixels from each micro-lens image to form a sub-aperture image. For example, the first pixel of the first micro-lens image becomes the first pixel of the first sub-aperture image. Then the first pixel of the second micro-lens image becomes the second pixel of the first sub-aperture image until the first sub-aperture image is made up of the first pixel from every micro-lens image. This is then repeated for the second pixel in each micro-lens images to create the second sub-aperture image and so on. Each of these sub-aperture images is an image of the scene with a slightly shifted parallax due to the differing angle of the incoming rays [7] [15]. In order to processes these sub-aperture images into a final image, a processing algorithm has to be used to combine these images. The final image has the same resolution as each of the sub-aperture images which is equivalent to the number of micro-lenses in the micro-lens array. Therefore, they more micro-lenses in your array, the higher the spatial resolution. Conversely, the smaller the micro-lenses are, fewer pixels are used behind each micro-lens. Since each pixel in the micro-lens image corresponds to a different incoming angle of the image, the fewer pixels behind each micro-lens, the lower the angular resolution.

Fresnel Zone Plates

The main optic of a plenoptic camera has traditionally used a lens to focus the incoming light, however a Fresnel zone plate also focuses light. Fresnel zone plates are based on the principles established in Fresnel diffraction theory. A Fresnel zone plate is a series of several radially symmetric rings used to create a diffractive optic. Each of the rings alternates between being optically transparent and optically opaque and are spaced such that the light transmitted through the transparent rings constructively interferes with each other at the point of the desired focus [16] [17] [18]. Therefore, the Fresnel zone plate uses diffraction instead of refraction or reflection that is used in lenses and mirrors. A sketch of a Fresnel zone plate is given in Figure 2 with the focal point labeled.

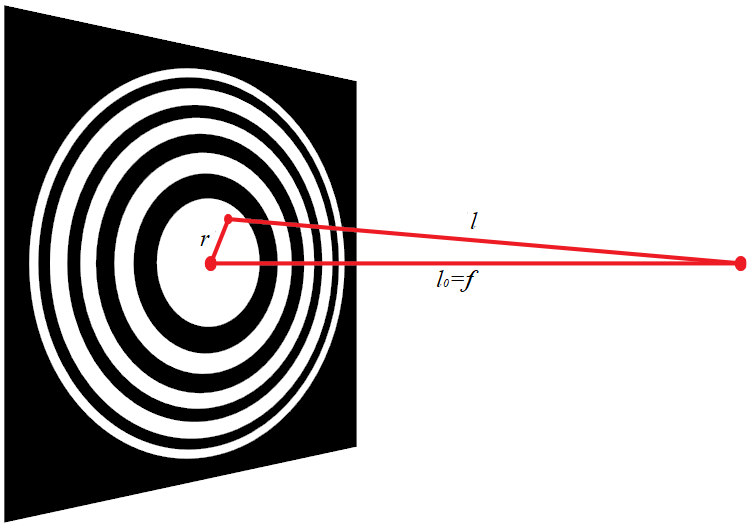

Figure 2. A drawing of a Fresnel zone with the focal point given as f.

In the Fresnel zone plate, the parts that are transparent have to constructively interfere. First, let l_0 be the distance to the focal point of the Fresnel zone plate from the

center of the first zone. Then, let *l* be the distance to the focal point from any other point on the zone plate. Since the entire first zone needs to constructively interfere, we need,

$$l - l_0 < \frac{\lambda}{2} \tag{1}$$

The second zone will be the location where destructive interference occurs and this happens where

$$\frac{\lambda}{2} < l - l_0 < \lambda \tag{2}$$

Since, this section destructively interferes, it is made opaque to block that section out. By continuing this pattern on, the n^{th} zone of the Fresnel zone plate can be generalized by the equation

$$\frac{(n-1)\lambda}{2} < l - l_0 < \frac{n\lambda}{2} \tag{3}$$

where *n* is a positive number from 1 to *N* (the total number of zones in the Fresnel zone plate). Here, all odd values of *n* will constructively interfere and will be transparent and all even values of n will destructively interfere with each other and will be opaque. The choice of the first zone as being the transparent zone is arbitrary and can be interchanged.

Despite which choice was made, the difference in the path length follows the limits placed by Equation (3). Therefore, the difference in path length between opaque and transparent zones is given by

$$l - l_0 = \frac{n\lambda}{2} \tag{4}$$

when compared with the center zone represented by the l_0. Note, that $f = l_0$ and that *l* can be represented by the Pythagorean theorem by letting the distance for the transition to the

n^{th} zone within the zone plate be called r_n. This can be thought of as the distance r for the n^{th} zone as represented in Figure 2. Inserting these substitutions back into Equation (4) gives us

$$\sqrt{f^2 + {r_n}^2} - f = \frac{n\lambda}{2} \tag{5}$$

Solving both sides of the equation for r_n gives us

$${r_n}^2 = n\lambda\left(f + \frac{n\lambda}{4}\right) \tag{6}$$

For the Fresnel zone plate that we will be using, f is large compared with $n\lambda/4$ so Equation (6) can be simplified to

$${r_n}^2 \approx n\lambda f \tag{7}$$

Equation (7) is true for the designed wavelength of the Fresnel zone plate, however, if we use a different wavelength of light than the design wavelength, the focal length will change. Note that the values for r_n and n were already chosen by our design of the Fresnel zone plate so they must remain constant with this calculation [16]. Therefore, the relationship between the focal length, f_λ, of a given wavelength, λ, can be represented by turning Equation (7) into a proportion in terms of f and λ to get

$$f_\lambda = \frac{f_0\lambda_0}{\lambda} \tag{8}$$

where f_0 is the design focal length for the design wavelength, λ_0.

As can be seen from Equation (8), the focal length of the Fresnel zone plate varies greatly with wavelength generating severe axial chromatic aberration. This is normally an undesirable characteristic, however, we can use it to our advantage by replacing the

main lens in a plenoptic camera with a Fresnel zone plate. We can take advantage of this axial chromatic aberration and use it in lieu of the range information gained from a traditional plenoptic camera [5].

Plenoptics with Fresnel Zone Plate

A FZP suffers from significant axial dispersion [16] [19] which, while normally a drawback, can be utilized to function as a spectrometer by scanning along the optical axis of the FZP with a detector to measure the spectral component irradiances of a source [20]. Additionally, the imaging resolution of a FZP and a refractive lens are similar when their sizes are the same [16]. It was recently shown experimentally that combining this spectral dispersion provided by a FZP with a plenoptic camera in order to create a diffractive plenoptic camera allowed the ability to conduct snapshot spectral imaging [21]. This setup was limited, however, in that it was mostly a proof of concept and did not determine the optimal algorithms to use for with this new snapshot spectral imager [21].

III. Processing Algorithms

Chapter Overview

A wave optics model was used in MATLAB to model the optical components and propagate the individual light rays as they passed through the system in order to accurately simulate the diffractive plenoptic camera. A thin lens approximation was used for the FZP with a varying focal length that depended on the wavelength. Additionally, only the rays that passed through the regions of the zone plate that were transparent were used to better model the FZP. The FZP was chosen to have a 30 mm diameter, a design wavelength of 800 nm, and a focal length of 500 mm at the design wavelength. The micro-lens array (MLA) was set at the focal length of the FZP at the design wavelength. These micro-lenses were simulated with 100 μm diameters and 8.31 mm focal lengths. The detector was placed at the focal length of the micro-lenses in accordance with the traditional plenoptic setup [14]. This process used the basic code from Hallada [21] with minor changes to the assumed size and positions of the lenses and added additional processing algorithms. For a full description of the basic computational algorithm, see the work by Hallada [22].

Four different algorithms were utilized in this work to process the data captured by the diffractive plenoptic camera. The first was a digital refocusing (DR) technique that is traditionally used with plenoptic cameras [7]. The second was a custom made Gaussian smoothing technique built from the basic DR algorithm. The third was a custom made super-resolution (SR) algorithm built based on the principles of other SR algorithms that utilize sub-pixel shifts in order to generate higher resolution images, but

designed around the diffractive plenoptic camera setup used here. The fourth and final algorithm was a Richardson-Lucy deconvolution algorithm that was built into the MATLAB software and had been used previously in other traditional plenoptic work [8].

Digital Refocusing

Ng developed the digital refocusing technique to refocus his plenoptic camera to different ranges [11]. Hallada applied this technique in order to refocus to different wavelengths [6] [21]. The DR technique takes each micro-lens image formed behind the micro-lenses and arranges them with the corresponding pixels in the other micro-lenses in order to form sub-aperture images. For example, the first pixel in the first micro-lens image is used as the first pixel in the first sub-aperture image. Then the first pixel in the second micro-lens image is used as the second pixel in the first sub-aperture image. This continues until all of the first pixels in all of the micro-lens images are used and the first sub-aperture image is formed. This is continued for the second pixel in all of the micro-lens images to form the second sub-aperture image and so on until all pixels are used for all of the sub-aperture images. This is represented in Figure 3.

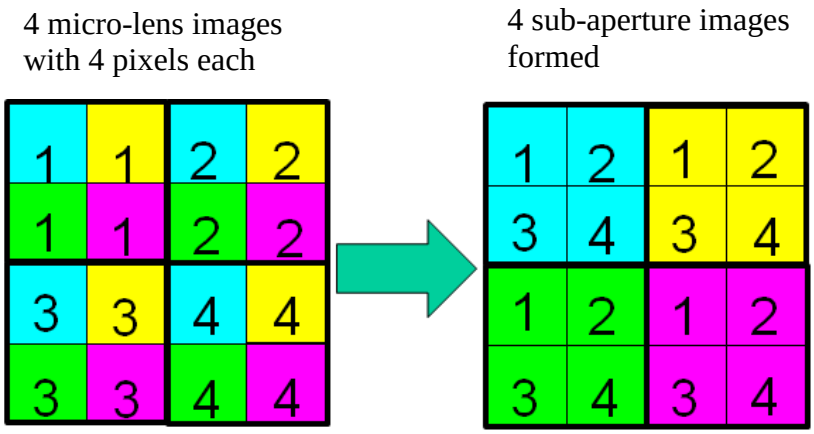

Figure 3. A graphical representation of the formation of the sub-aperture images in the DR algorithm. Each pixel behind each microlens is combined in the order shown to generate a sub-aperture image. These sub-aperture images are then aligned with each other by shifting and are then averaged together to form a final, digitally refocused image.

After the sub-aperture images are formed, each of the sub-aperture images are shifted based on the parallax of each image being formed at a slightly different angle based on the different positions of the micro-lenses in the MLA and the wavelengths used. The formula for the shift in a given direction is

$$shift = \left(\frac{\frac{2m-1}{2} - \frac{M}{2}}{M} \right) \left(\frac{ZP_d}{ML_d} \right) \left(1 - \frac{ZP_f}{ZP_{f-act}} \right) \tag{9}$$

where M is the total number of pixels in the sub-aperture image in the direction that the shift is occurring, m is the pixel number in that direction counting from the edge of the sub-aperture image, ZP_d is the diameter of the zone plate, ML_d is the diameter of the micro-lens, ZP_f is the focal length of the zone plate at the design wavelength, and $ZP_{f\text{-}act}$ is the focal length of the zone plate at the wavelength being examined. After each image is shifted, all of the sub-aperture images are averaged together in order to produce a final

image. An estimate for the spectral range able to be perfectly refocused can be calculated from Ng's Fourier analysis of digital refocusing with plenoptic cameras [23]. By combining the relation he forms with Equation (8), we get

$$\lambda_{cutoff} = \frac{\lambda_0}{1+\frac{\Delta x}{\Delta u}}, \tag{10}$$

where $\lambda_{cuttoff}$ is the minimum wavelength for perfect digital refocusing, λ_0 is the design wavelength of the FZP, Δx is the spatial sampling rate given by the number of pixels per micro-lens image, and Δu is the angular sampling rate given by the ratio of the diameter of the zone plate to the diameter of the micro-lenses. For the modeled system, the range of perfect digital refocusing will extend down to 770 nm from the 800 nm design wavelength. Since two of the other algorithms, Gaussian smoothing and SR, are built on the same concepts as the DR algorithm, they both have the same restrictions and this "perfect range" also applies to them.

Gaussian Smoothing

In the Gaussian smoothing technique used here, the sub-aperture images are formed from the raw data in the same method as for the DR method. After the sub-aperture images are formed, the middle sub-aperture images are used to form the final image. In general, the center nine by nine block of sub-aperture images were used, however, three by three and five by five sets of images were used as well which provided much faster computation time for a lower image pixel count. This removes the outside pixels of each micro-lens image or, thought about a different way, removes the outside

images of each of the sub-aperture images. This method removes the worst quality pixels from the final image and thus, if the outside pixels that were recorded are of particularly poor quality, they can be dropped to improve the quality of the final image. After the center sub-aperture images are chosen, the images are lined up based on the geometry of the plenoptic setup and the wavelengths used as in the DR method and then the corresponding pixels are stitched together again to form a mosaic of all of the sub-aperture images used. This forms a higher pixel count image than the DR algorithm since the each of the individual pixels from the used sub-aperture images are maintained rather than being averaged together. Therefore, if an N x N set of sub-aperture images is used, the final image pixel count becomes N^2 times that of the DR algorithm. This higher pixel count mosaic is then smoothed with a Gaussian function to form a final image. A graphical description of this method is provided in Figure 4.

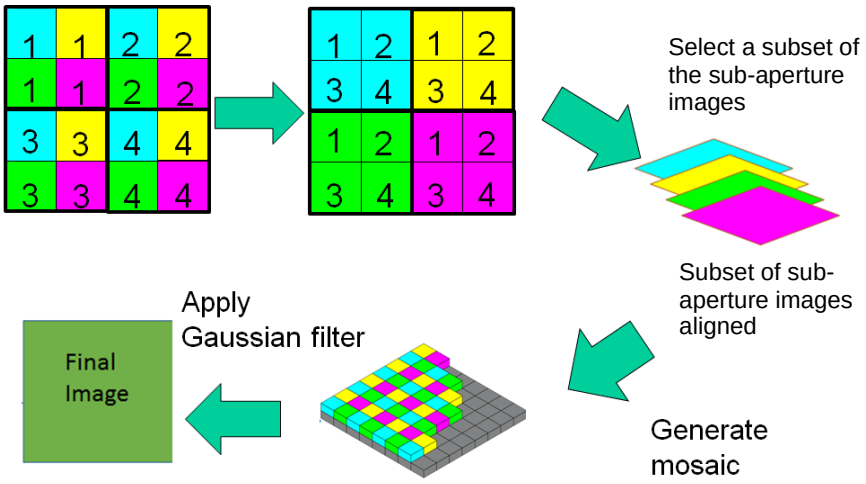

Figure 4. A graphical representation of the formation of the final image in the Gaussian smoothing algorithm after the creation of the sub-aperture images. After the sub-aperature images are formed, as in DR, they are aligned. However, we only used the center 9x9 sub-aperture images. The same process used to take the micro-lens images into sub-aperture images is then done again to form a mosaic of the sub-aperture images. A Gaussian filter is then applied to the mosaic to give the final image from the Gaussian filter algorithm.

Super-Resolution

Super-resolution is a method in which, through various methods of post processing an image, you are able to increase the resolution beyond the limits of the imaging equipment used. This method is traditionally used to provide an increased spatial resolution by combining multiple images of the same scene and seeing how the measured pixel response changes over sub-pixel shifts of the scene [24] [9] [10] [25]. The idea of super-resolution has already been applied to satellite imaging and medical imaging along with many other applications where multiple images can be taken [24] [26].

In the SR algorithm used here, the shifted sub-aperture images are the collection of images used. The sub-aperture images were formed the same way as described for the DR algorithm. Then the center sub-aperture images were used to form the final image as it was in the Gaussian smoothing algorithm. In general, the center five by five images were used but the center three by three and center nine by nine images were also occasionally used. This allows for customization into the number of pixels of the final image much as in the Gaussian smoothing algorithm. However, in this method, after the actual shift needed for each sub-aperture image was calculated, instead of shifting all of the images to line them up, each pixel was assigned a location based on its pixel location with the shift, calculated in pixels, added to that location. The formula for the shift in a given direction is the same as in Equation (9) except here, the full sub-pixel shift is kept. A final image is then formed by placing each pixel at its exact assigned final location and then performing a linear interpolation between each of those pixels with a chosen pixel count ten times the original.

Deconvolution

The final algorithm utilized was the Richardson-Lucy Deconvolution algorithm. The need for better performance led to the development and application of the deconvolution method, based on wave optics, for 3-D microscopy [8] and was determined to perform better than the DR method for a traditional plenoptic camera [27]. In the deconvolution algorithm, the standard deconvolution command was used in MATLAB that utilizes the Richardson-Lucy method. The Richardson-Lucy deconvolution algorithm takes advantage of the fact that a non-point source is effectively the sum of many point sources [28]. The iterative method can be written as

$$d_i = \sum_j p_{ij} u_j , \tag{11}$$

where d_i is the observed value at the pixel location i, p_{ij} is the point spread function and the fraction of light from j that is observed at i, and u_j is the pixel value at j. Equation (11) is then solved by calculating the most likely u_j given an observed d_i with a known p_{ij} [28]. This gives us an iterative equation

$$u_j^{(t+1)} = u_j^{(t)} \sum_i \frac{d_i}{c_i} p_{ij} , \tag{12}$$

where

$$c_i = \sum_j p_{ij} u_j^{(t)} , \tag{13}$$

Equation (12) is then solved through an iterative process by using the values calculated from Equation (13). Here, the point spread function is calculated beforehand and is given by

$$F(\mathbf{s}) = \int\int h^2(\mathbf{s}, \lambda, \mathbf{p}) E(\lambda, \mathbf{p}) d\lambda d\mathbf{p} , \tag{14}$$

where F is the irradiance at a position s on the detector, h^2 is the point spread function for a single detector location at object point p and wavelength λ, and E is the actual spectral irradiance being imaged, evaluated at a specific wavelength and spatial location [5]. A full description of the Richardson-Lucy algorithm has been described by Lucy [28].

The Richardson-Lucy deconvolution algorithm was used with as few as 10 iterations to as many as 1000 iterations in this paper, however, 400 iterations was used as the standard comparative setting. Utilizing more iterations increases the quality of the images, to a point, at the cost of computation time.

IV. Results

Chapter Overview

Each of these algorithms was run many times to determine the optimal case for the use of each algorithm. The results here look at the simulations run for single and multiple wavelengths emitted at a time while looking over the 400 nm to 850 nm range. The main image used for these tests is the 1951 USAF resolution test chart as seen in (a) of Figure 5, however, several other images were used in order to get a better idea on the real-world performance of the algorithms. In each of the simulations, the angular resolution corresponding to the bars for each of the sections on the chart were calculated with the values of the corresponding bars given in (b) of Figure 5. In this chart, an observer can look and see if they can see all three bars in a group. If they are able to see all three bars, then the grouping is considered resolved. In order to compare the results more quantitatively instead of qualitatively, the image modulation depth (IMD) was used as a metric. This is calculated by taking one of the sets of bars on the charts and assigning whether each pixel is supposed to be a light pixel or a dark pixel based on its location. The IMD is then calculated based on the formula,

$$IMD = \frac{light-dark}{light+dark}, \tag{15}$$

where the light value is based on the average measured value of all pixels that should be light and the dark value is the average of the measured value for all the pixels that should be dark [29]. In addition to the resolution chart, point sources were also examined in order to more clearly see the effects of changing wavelength and algorithm.

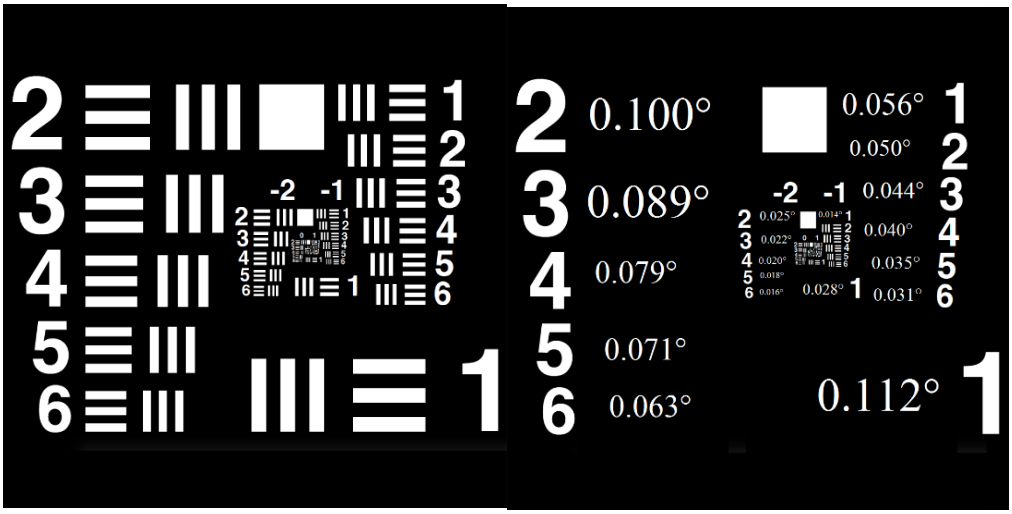

(a) (b)

Figure 5. The 1951 USAF resolution chart used for simulating the results of the diffractive plenoptic camera is shown in (a). The same chart but providing the angular resolution of each section of the chart for our simulation setup is shown in (b).

Single Wavelength Resolution Chart Results

When the algorithms are run with a single wavelength generating the image near the design wavelength of 800 nm, the results are all very similar. This makes it so the full images are too similar to see a difference. Therefore, Figure 6 provides a zoomed in image of the fourth smallest "1" in the USAF target image with each of the four algorithms run at 795 nm. From a subjective viewpoint, the super resolution algorithm and deconvolution algorithm show an improvement over the traditional digital refocusing algorithm with the deconvolution algorithm giving the best quality. The Gaussian algorithm does not provide any additional resolution over the digital refocusing algorithm as measured by the IMD, however, the smoothing that happens on the sharp edges of the number, for example, provide a subjectively better quality image on the numbers next to the bars.

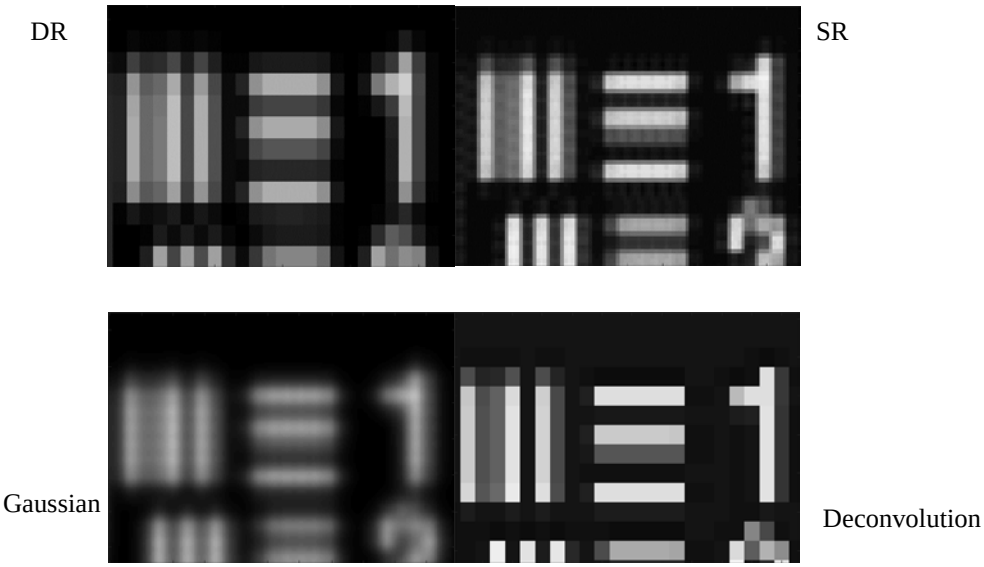

Figure 6. The diffractive plenoptic camera results simulated with 795 nm light with a the image zoomed on the fourth 1 of the USAF target with DR in the top left, SR in the top right, Gaussian smoothing in the bottom left, and deconvolution in the bottom right run with 400 iterations. This is one of the smallest groups able to be resolved by the algorithms and shows the differences in quality for the different methods even though all are considered resolved at this level.

In order to provide an objective comparison between the quality of the images produced by the different algorithms, an image modulation depth (IMD) was used as well as a calculation of the angular resolution that each algorithm was able to provide. After testing, it was determined that a calculated IMD of 0.03 provided results that matched objective views of the angular separation being resolved so that value was used as the limit for whether a given angular separation was able to be resolved. Figure 7 shows the angular resolution provided by each algorithm in 25 nm increments from 400 nm to 775 nm with an additional data point given at 795 nm. The deconvolution results are split into five cases with the number of iterations varying from 10 to 400. Above the 770 nm wavelength that provides perfect digital refocusing, all algorithms reached the same "perfect" angular resolution of 0.0099°. As the wavelength gets farther from the FZP's

design wavelength of 800 nm, the angular resolution worsens except for the deconvolution algorithm with 400 iterations that was able to produce images with the same angular resolution at all wavelengths shown. The deconvolution algorithm run with only 10 iterations resulted in the worst results showing that 10 iterations is not enough to keep up with the other algorithms outside the perfect digital refocusing range. Within the other three algorithms, the super resolution algorithm consistently performed as well as or better than the digital refocusing algorithm. The Gaussian smoothing algorithm performed similarly to the digital refocusing algorithm with most of the data points falling within the error bars. The standout performer was, by far, the deconvolution algorithm. If time was available to run the full 400 iterations, image quality similar to the images produced at the design wavelength were possible at any wavelength tested. The more iterations used, the farther from the design wavelength the angular resolution was maintained. Note that there is a fundamental limit at 0.01° for the angular resolution. This is due to the fact that at this resolution, the bar grouping on the chart only has exactly five pixels to represent the three dark and two light lines. Beyond that limit, there are fewer pixels available than lines.

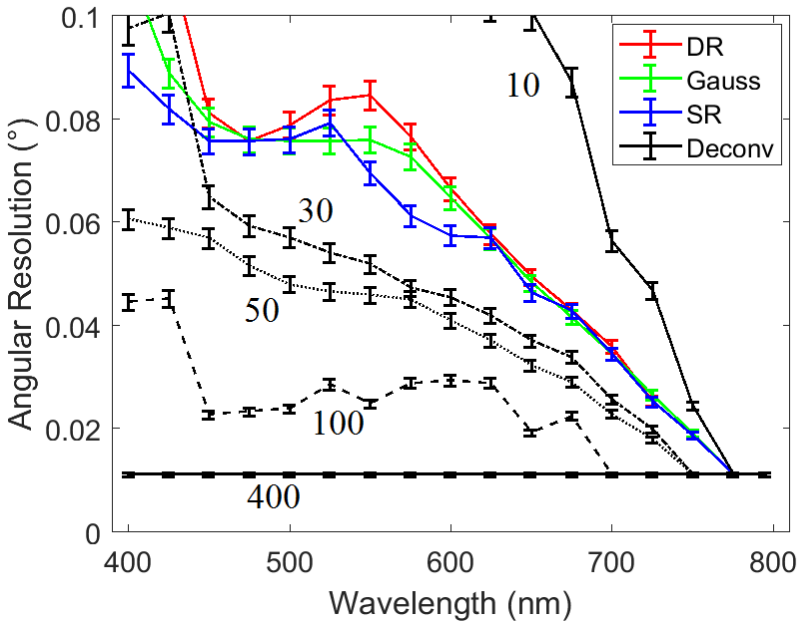

Figure 7. The diffractive plenoptic camera results showing the angular resolution at a given wavelength. All of the deconvolution results are shown in black with the number of iterations used displayed next to the corresponding line. The SR algorithm was able to provide a better or similar angular resolution than the DR algorithm for all wavelengths tested with similar computational time. The deconvolution algorithm provided the best angular resolution in all cases if enough iterations were used at the cost of a large amount of computational time. The Guassian smoothing algorithm did not show a large improvement in angular resolution over the DR algorithm despite requiring a large computational investment.

Since each three bar element on the USAF target corresponds to a different angular resolution, we can calculate the IMD at each of those elements. Figure 8 shows the IMD at each location on the chart for the DR, SR, and Gaussian algorithms along with the deconvolution algorithms run at 10, 30, 50, 100, and 400 iterations for 795 nm, 750 nm, 700 nm, and 500 nm light. When close to the design wavelength, 10 iterations is enough for the deconvolution algorithm to get results similar to design so all five deconvolution lines fall on top of each other for the first image. Varying the number of iterations provides separation farther from the design wavelength, however, and while the 100 and 400 iteration runs are close at 750 nm, as the wavelength simulated gets farther from the

design wavelength of 800 nm, the separation becomes more pronounced. Meanwhile, the super resolution algorithm outperforms the digital refocusing and Gaussian smoothing algorithms near design. Farther from the design wavelength, however, all three algorithms become very poor and are indistinguishable from one another. The Gaussian smoothing algorithm performs slightly better than the digital refocusing algorithm at larger angular separations and slightly worse at smaller angular separations. This is due to the smoothing algorithm smoothing the bars together when the angular separations get small enough. Even though the numbers next to the bars looks better, the IMD is worsened due to the smoothing. By the time we get to 500 nm, which is 300 nm from the design wavelength, only the 400 iteration deconvolution algorithm performs well. All other algorithms, as well as using the deconvolution algorithm with fewer iterations, are unable to resolve the chart well beyond about 0.04° of angular separation. The deconvolution algorithm, using 400 iterations, is able to resolve similarly at any of the angular separations measured with the target.

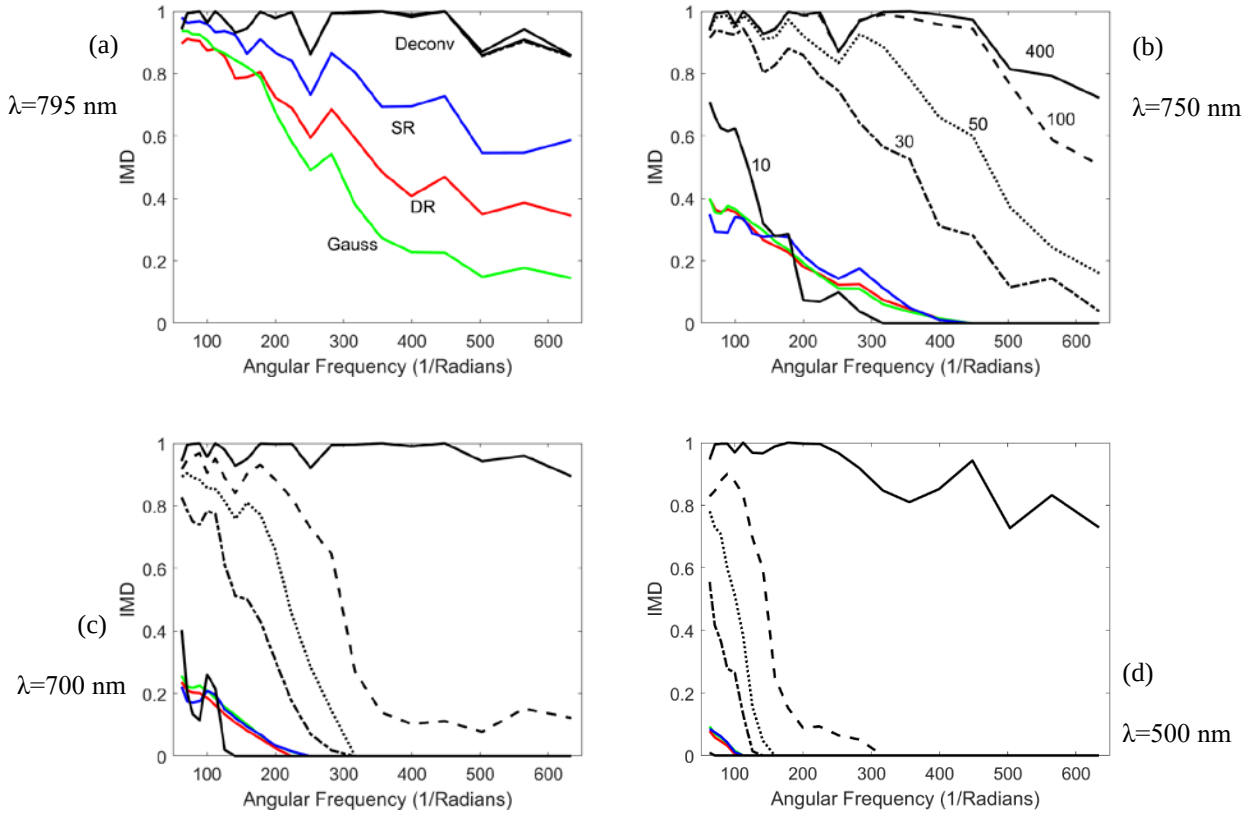

Figure 8. The diffractive plenoptic camera results of the USAF target, simulated with 795 nm light on top left, 750 nm light on top right, 700 nm light on bottom left, and 500 nm light on bottom right. All of the deconvolution results are shown in black with the number of iterations differentiated by various dotted, dashed, or solid lines labeled in the second image and the SR, Gaussian, and DR algorithms are labeled accordingly in the first image. Deconvolution with 400 iterations is able to maintain it's same resolution at all wavelengths test while the other algorithms, including the deconvolution run with fewer iterations, is unable to resolve large angular frequencies far from the design wavelength of the Fresnel zone plate.

Simulated Noise

A simulated Gaussian noise source was added to the measured images in order to verify that the deconvolution algorithm could still use a large number of iterations on these single wavelength results even with noise since the deconvolution algorithm requires a large number of iterations when far from the design. Simulations were run with SNR values ranging from 1 to 100 with the deconvolution using up to 1000

iterations. Throughout the runs, if the SNR was above 5, the deconvolution algorithm performed as expected in all tested cases. However, as the SNR was lowered to 5 and below, some runs of the deconvolution algorithm would almost completely clear out the entire image. Additionally, if the noise caused an incorrect step in the iterative process, the algorithm almost immediately cleared the entire image and processing more iterations past that point did not return the image. The algorithm failed in testing between 150 and 550 iterations in all the cases tested that resulted in a failure.

The deconvolution algorithm, however, converges to the solution very quickly when near design; as seen in Figure 8. Therefore, the larger numbers of iterations are only necessary when far from design. When near design, 795 nm, 70% of the deconvolution runs failed before the 1000 iterations chosen was completed. This failure was displayed by the iterative deconvolution algorithm eventually producing a blank or near blank image instead of reproducing a noisy target chart. When the deconvolution algorithm with noise was tested far from design at 500 nm, none of the deconvolution runs failed by 1000 iterations. An example run is shown in Figure 9 that shows the same target run with the same seeded simulated Gaussian noise at SNR 1. Since the cases where noise caused the deconvolution algorithm to fail were only for light close to the design, the requirement to limit the number of iterations in those cases are not a problem since not many iterations were needed before the best results were produced. It should be noted that the measured IMD values in these high noise runs were significantly decreased versus the runs without noise in all of the successful runs, but this is expected with such high noise values. It should also be noted that noise was added to the other algorithms as well but no significant changes occurred with those methods. The results were simply

noisy versions of the original image as expected. It should also be noted that the other simulated noisy runs all looked similar to Figure 9 where all the runs that failed looked similar to (a) and the ones that didn't fail looked like (b) with runs with larger SNR simply appearing less noisy so Figure 9 is representative of the noise tests ran.

(a) (b)

Figure 9. The diffractive plenoptic camera results simulated with (a) 795 nm light and (b) 500 nm light and simulated Gaussian noise with an SNR of 1 and with both images refocused at their respective wavelength utilizing the deconvolution algorithm with 1000 iterations. Both algorithms used the same seed for the randomly generated noise and the same number of iterations, yet the image that was emitted near the design wavelength was unusable, while the one rendered far from the design wavelength is still recognizable.

Point Sources

In order to more clearly see how varying the wavelength separation from the FZP's design affects the efficacy of each of the algorithms, point sources were simulated at various wavelengths and each of the refocusing algorithms was applied to the images formed. This tells us the relative spread of point sources that are in or out of focus and their spectral resolution. Figure 10 shows the results after a 795 nm point source was simulated shining on our diffractive plenoptic camera and then all four algorithms were

employed. This is only 5 nm off the design wavelength of 800 nm. All the algorithms performed well in the simulation. The effects of the higher pixel counts available to the SR and Gaussian smoothing algorithms is apparent in these well focused images. These higher pixel counts allow both of these algorithms to produce results that appear more like a point source than the pixelated versions visible in the DR and deconvolution algorithms. This close to the design, however, the point sources were rendered accurately by all algorithms which confirms our results that we already saw with other images in Figure 8.

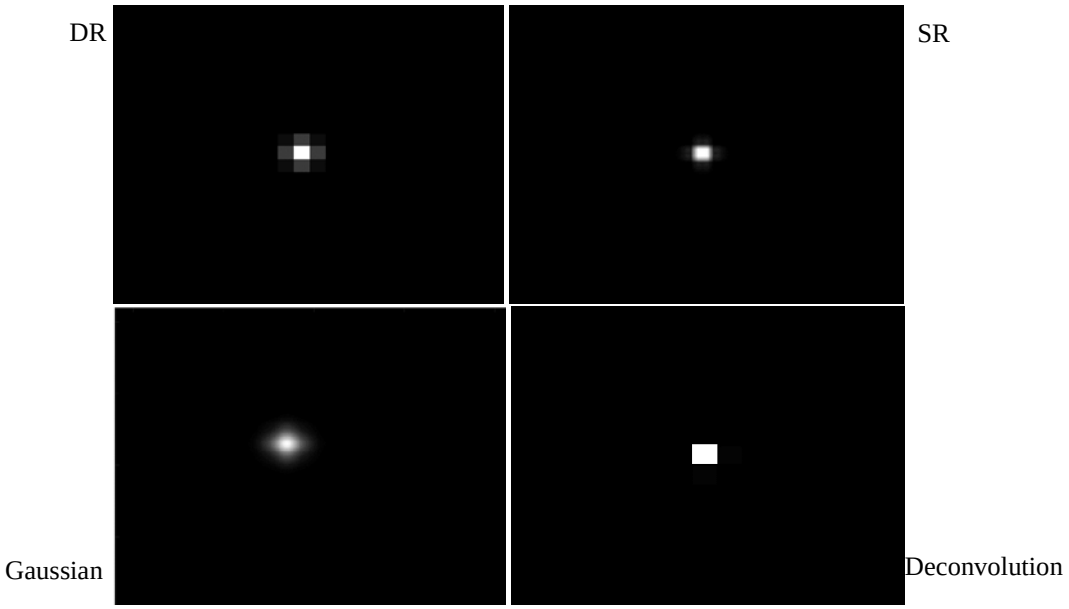

Figure 10. The diffractive plenoptic camera results simulated with 795 nm point source (5 nm off design) with DR in the top left, SR in the top right, Gaussian smoothing in the bottom left, and deconvolution in the bottom right run with 400 iterations. All results were refocused at 795 nm and are shown at the same scale. There is not a large difference between the algorithms at this close to the design wavelength, however, the increased pixel count of the SR and Gaussian smoothing algorithms allow for a more rounded (and more accurate) point source than the square point sources rendered by the DR and Deconvolution algorithms.

We then changed the simulated point source to emit at 545 nm, as seen in Figure 11. This is now 255 nm off design. Here the results change drastically. The deconvolution

algorithm, run with 400 iterations, is able to reproduce the results from near design. The other three algorithms are all unable to adequately refocus this far off design. The DR and Gaussian smoothing algorithms produce similar results with the same spread, however, once again, the higher pixel count provided by the Gaussian smoothing method provides a less aliased view. The super resolution method performs very poorly here becoming very pixelated.

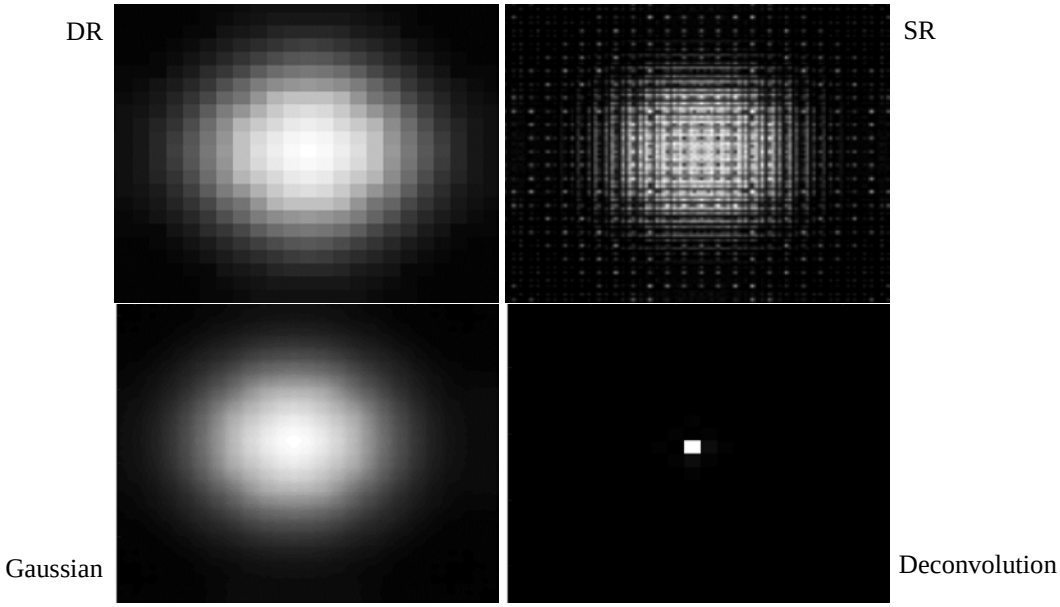

Figure 11. The diffractive plenoptic camera results simulated with 545 nm point source (245 nm off design) with DR in the top left, SR in the top right, Gaussian smoothing in the bottom left, and deconvolution in the bottom right run with 400 iterations. All results were refocused at 545 nm and are shown at the same scale. Note that the point source rendered by the deconvolution algorithm appears identical to the run near design while all of the other algorithms have large amounts of blurring.

One of the benefits of the diffractive plenoptic camera moving the range information into the wavelength domain is the ability to refocus on specific wavelengths. To start, we use a wavelength near design where all the algorithms worked well. Figure 12 is the result of the same input data as Figure 10, that is a 795 nm point source, however, the

refocusing algorithms are trying to refocus at 780 nm instead, a full 15 nm difference from the point source. Here you get poor results from all of the methods which is what is wanted. This tells us that the wavelength we have refocused on is the wrong wavelength. In the DR, SR, and Gaussian smoothing algorithms, however, there are still some visible images which can be difficult to differentiate from much dimmer point sources in the case of DR, or several dimmer point sources in the Gaussian smoothing and SR techniques. The deconvolution technique, however, gives us precisely what is desired which is no visible result when refocused at the incorrect wavelength.

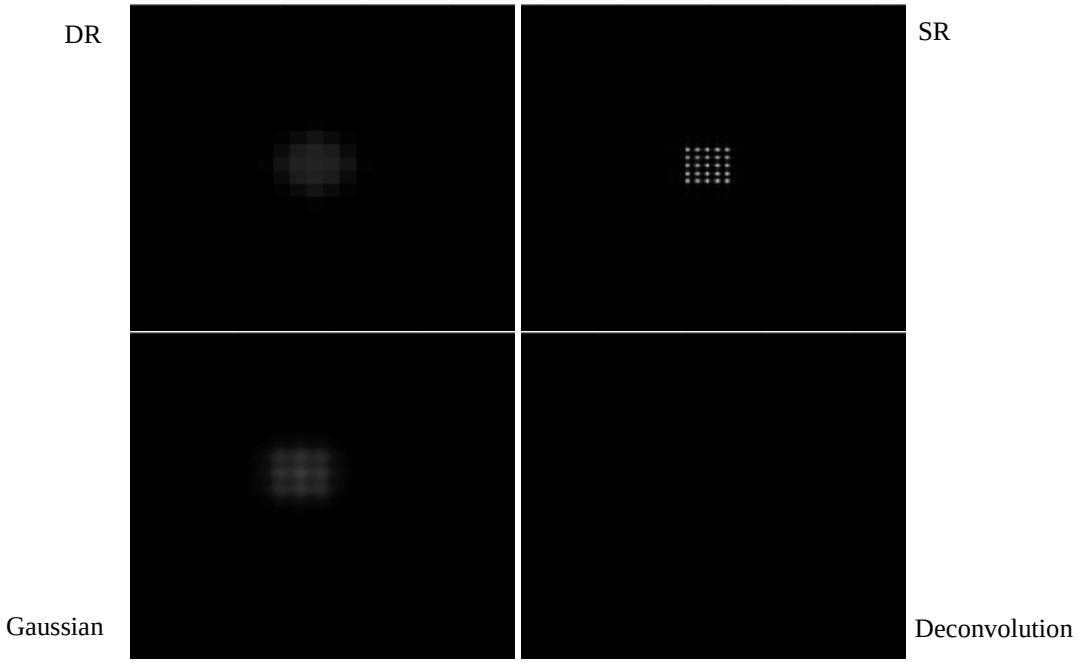

Figure 12. The diffractive plenoptic camera results simulated with 795 nm point source (5 nm off design) with DR in the top left, SR in the top right, Gaussian smoothing in the bottom left, and deconvolution in the bottom right run with 400 iterations. All results were refocused at 780 nm (15 nm off source wavelength). All images are scaled to match the brightness of the corresponding algorithms in Figure 10. Note that the deconvolution results are not visible which would be the optimal result showing that we are refocusing on the wrong wavelength that the source is not emitting at. The other algorithms all produce images much dimmer than when refocusing on the correct wavelength, however, there are still visible elements that could cause a false positive reading.

We then do the same for a point source that is far from design where the results were poor for the three methods based on digital refocusing but good for deconvolution. Figure 13 is the result of the same input data as Figure 11, that is a 545 nm point source, however, this time, the refocusing algorithms are trying to refocus at 530 nm instead. A 15 nm difference from the point source again. Here, the images for DR, SR, and Gaussian smoothing look similar to when we refocused to the correct wavelength. This means that when the sources are far from design, we are unable to determine an exact wavelength of the source if we are using one of these algorithms. The deconvolution algorithm works the best here with a barely visible image when refocusing on the incorrect wavelength.

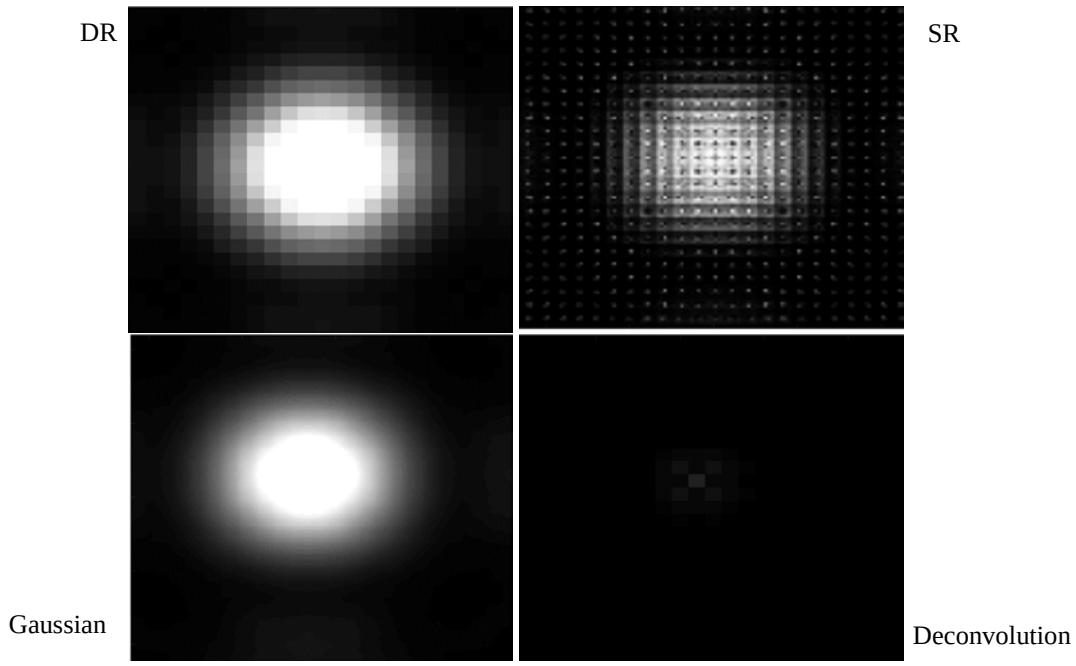

Figure 13. The diffractive plenoptic camera results simulated with 545 nm point source (245 nm off design) with DR in the top left, SR in the top right, Gaussian smoothing in the bottom left, and deconvolution in the bottom right run with 400 iterations. All results were refocused at 530 nm (15 nm off source wavelength). All images are scaled to match the brightness of the corresponding algorithms in Figure 11. Note that the deconvolution results are barely visible which shows that we are refocusing on the wrong wavelength that the source is not emitting at. The other algorithms all produce images similar to the image when refocused at the correct wavelength which means we are unable to tell which wavelength is the correct wavelength that the source is emitting at.

Relative Energy, Grayscale, and More Complicated Images

All of the results shown thus far have been binary. That is, the simulated source was either all the way on or all the way off. In order to ensure that all algorithms maintain the correct relative energies, four different aspects were examined. First, we verified that a source displayed near the center of the sub-aperture images maintained the same brightness near the edge of the sub-aperture images. Second, we verified that sources with the same brightness but different wavelengths were measured the same. Third, we verified that a source that was fractionally as bright was displayed by the algorithms with the correct brightness ratio. Finally, we looked at recording a more complicated image with multiple small scale features and varying brightness to ensure that the algorithms performance with the point sources was repeated.

For sources that were positioned such that they fell at the edge of the sub-aperture images, the relative irradiances were not necessarily maintained. The relative irradiances of 745 nm point sources near the edge of the sub-aperture images, near the center of the sub-aperture images, and in between when the image is refocused at different wavelengths from all four algorithms are shown in Figure 14. Note that when using the DR algorithm, the relative irradiance detected for point sources near the edge of the sub-aperture images were only a third of those near the center despite the point sources all being identical. The curve, however, is smooth and regular which is desired. Note that only two lines can be seen on the graph. This is because the three middle points are all on top of each other and the two edge points are on top of each other. The Gaussian

smoothing algorithm produced similar results to the DR algorithm, however, when the point source falls right near the edge of the sub-aperture images, the Gaussian smoothing pushes some of the irradiance off of the edge and so even more of the irradiance is lost if the point source falls on the very edge of a sub-aperture image. Otherwise, the Gaussian smoothing algorithm is also very smooth and similar to DR. Once again, the three middle points all produced identical results so their curves are on top of each other. The SR algorithm corrected the problem where the relative irradiances were not maintained based on location. The measured irradiance was the same regardless of the location in the sub-aperture images that the point sources fell. Unfortunately, the irradiance recorded when refocusing at different wavelengths is not very smooth and this can lead to a false detection of point sources at different wavelengths than was actually used. This is due to the fact that the since the SR algorithm does not average the sub-aperture images together, that the small variations visible in each sub-aperture image that is averaged out in the DR algorithm, are still displayed in the SR algorithm. Finally, while the deconvolution algorithm did not maintain the relative irradiances of the point sources perfectly, it did much better than the DR algorithm. The deconvolution algorithm maintained the relative irradiances as not less than 70% of the measured irradiance of the point source near the center of the sub-aperture image. The deconvolution algorithm also had an issue when near design with some false positives near design picked up. This can make determining the wavelength and even existence of sources at wavelengths close to the design wavelength of the FZP difficult. This is due to the fact that since the difference in the incident angle of different wavelengths near design is smaller, the deconvolution algorithm has a harder time separating them.

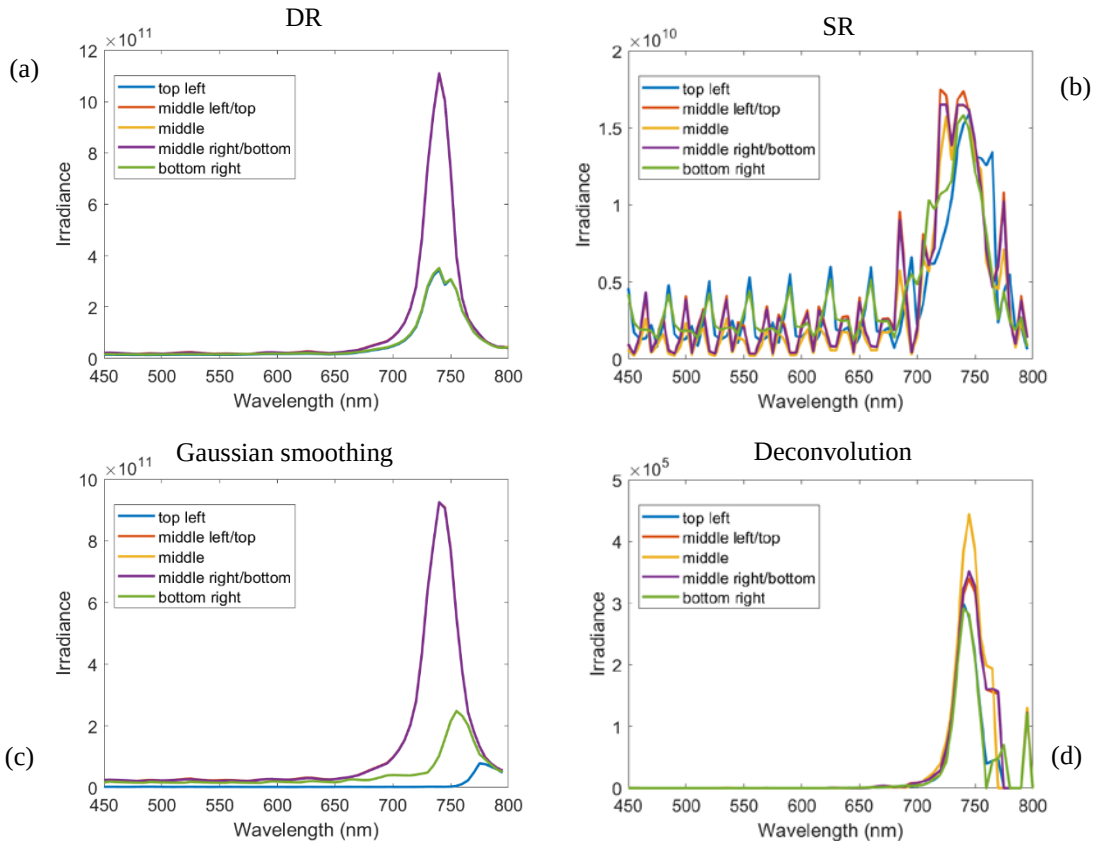

Figure 14. The diffractive plenoptic camera relative irradiance detected when refocused at different wavelengths from identical simulated 745 nm point sources that fall on the sub-aperture image either on the top left, bottom right, middle, or in between those three points. Image a) is DR, b) is SR, c) is Gaussian smoothing, and d) is deconvolution. The DR and Gaussian smoothing both lost irradiance from measurements near the edge pixels. The SR doesn't lose the irradiance, however, it suffers from irregularly oscillating features. Deconvolution corrects most of the issues of lost irradiance near the edge, however, it suffers from false positives near the design wavelength. Note that for DR, the curves representing the three middle lines all fall on top of each other while the curves representing the two edge lines fall on top of each other. Similarly, for the Gaussian smoothing algorithm, the curves representing the three middle lines all fall on top of each other as well.

For completeness, the data from Figure 14 were run again for 545 nm point sources and displayed in Figure 15. Since the incident angle of the incoming point source is larger due to the larger diffraction of the FZP, more sub-aperture images lose the point sources that appear near the edge. Therefore, when the DR algorithm takes those sub-aperture images and averages them together, several of them will be missing the edge

point sources and the relative irradiances are even farther from what is measured near the center of the sub-aperture images. This can be seen in Figure 15 with point sources at 545 nm displaying at less than 25% of the point sources near the center for both the DR and Gaussian smoothing algorithms. However, we see that the relative widths of the irradiance curves are much larger than they were for the 745 nm point sources which makes determining the exact wavelength of the light without a priori knowledge of the source much less exact. The SR algorithm is still able to maintain the relative energies as well at 545 nm as it was at 745 nm, however, it also still had the same variation that we saw in the 745 nm test as well. The deconvolution was able to maintain the relative irradiance even better at 545 nm than it was at 745 nm. The relative energies were within 15% of the measured irradiance at any location. Additionally, the irradiance curve is much thinner than the other methods and this allows a more accurate determination of the source wavelength than the other methods at this wavelength. As the source is farther from the design wavelength, it also does not suffer from the same variation that we saw near the design wavelength in Figure 14.

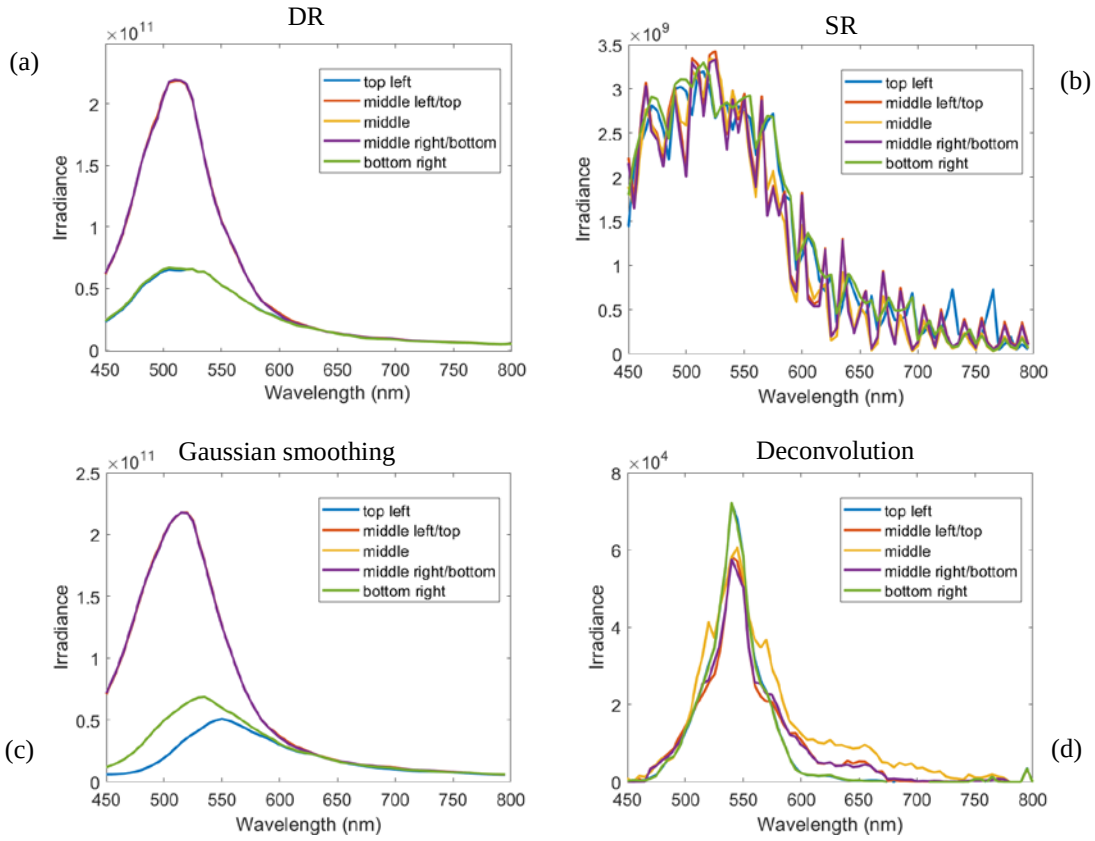

Figure 15. The diffractive plenoptic camera results of the relative irradiance detected from identical simulated 545 nm point sources that fall on the sub-aperture image either on the top left, bottom right, middle, or in between those three points. Image a) is DR, b) is SR, c) is Gaussian smoothing, and d) is deconvolution. The DR and Gaussian smoothing both lost irradiance from measurements near the edge pixels. The SR doesn't lose the irradiance, however, it suffers from irregularly oscillating features. Deconvolution corrects most of the issues of lost irradiance near the edge and doesn't suffer from the false positives that it did near the design wavelength. The DR, SR, and Gaussian smoothing algorithms all have a large FWHM curve while the deconvolution algorithm shows a much small FWHM representing a much more accurate estimation of the source wavelength. Note that for DR, the curves representing the three middle lines all fall on top of each other while the curves representing the two edge lines fall on top of each other. Similarly, for the Gaussian smoothing algorithm, the curves representing the three middle lines all fall on top of each other as well.

The relative energies were not only checked based on the location of identical point sources, but also when the point sources had varying wavelengths. A plot of the measured irradiance when refocusing at various wavelengths is shown for all four algorithms and for six different point source wavelengths in Figure 16. None of the algorithms were able to successfully keep the relative irradiances the same when looking

at different point sources. The DR and Gaussian smoothing algorithms are very similar to each other. Note that, once again, we see further verification that the irradiance spreads out in the refocused wavelength as we get farther from the design wavelength of the FZP. This is true for the DR, SR, and Gaussian smoothing algorithms. The deconvolution algorithm, however, is able to maintain a very tight spread in wavelength space as we get farther from the design wavelength of 800 nm. In fact, the spread decreases as the point source wavelength gets farther from design allowing for more accurate determination of the wavelengths of the sources. The SR algorithm's variation makes it hard to differentiate between the sources since the overlap is so bad. Finally, the relative irradiances do start to match up better once we drop below about 650 nm for our source (or 150 nm from the design of the FZP) for all algorithms. This tells us that we can better maintain relative brightness and more accurately represent the irradiance values of different wavelength sources when far from design.

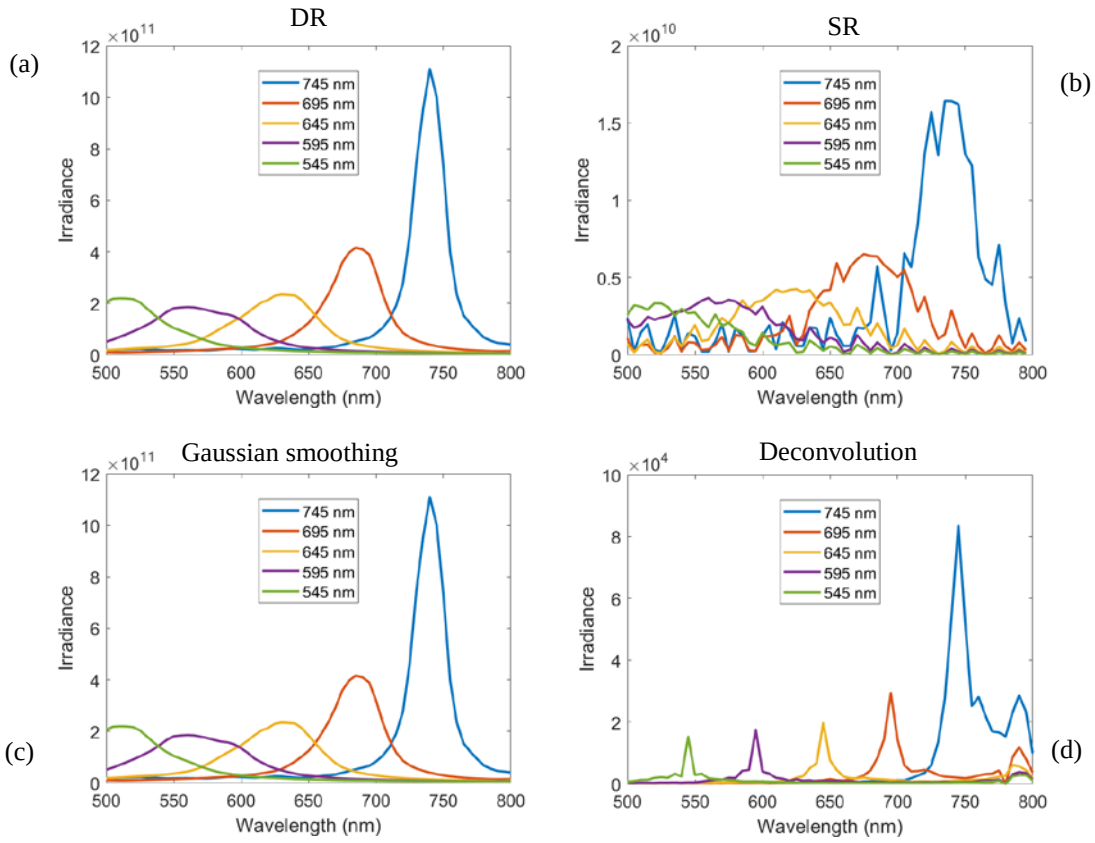

Figure 16. The relative irradiance by wavelength refocused from six different simulated point sources with the given wavelengths all at the same relative brightness. Image a) is DR, b) is SR, c) is Gaussian smoothing, and d) is deconvolution. The DR, SR, and Gaussian smoothing curves are similar in size and shape demonstrating that that they provide similar wavelength resolution. Each of them, however, have the curves' FWHM values increase as the wavelength gets farther from the design wavelength representing worsening wavelength resolution. Deconvolution, however, has very small FWHM curves with the values even decreasing as the emitted wavelength gets farther from design.

Next, we looked at the relative energies of grayscale point sources. In Figure 17, we examine point sources with 10%, 25%, 50%, and 100% brightness levels, all emitting at 795 nm, and all refocused at 795 nm. The horizontal scale of the images has been normalized for the varying number of pixels in each of the different algorithms to represent the relative size of the point source. All four algorithms were able to maintain the relative irradiance values for a grayscale point source. At 795 nm, we see all four algorithms performing well at displaying a very small and tight point source. The DR

and Gaussian smoothing algorithms both performed the same with the only difference being the Gaussian smoothing algorithm's curve being smoother due to the increased pixel count that that algorithm has. The SR and deconvolution algorithms are both the most localized with the SR algorithm slightly edging out the deconvolution algorithm when only 5 nm from design.

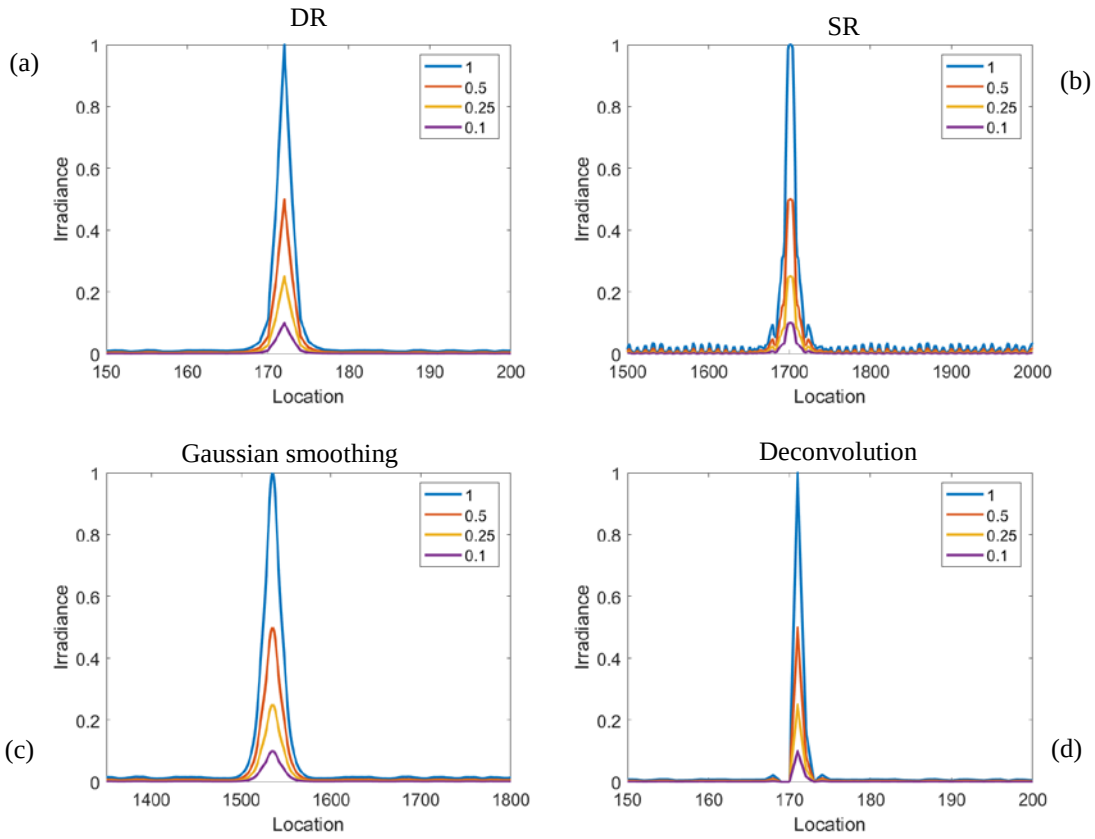

Figure 17. The relative irradiance by pixel location on the refocused image detected from a simulated point source at 795 nm point sources that with 10%, 25%, 50%, and 100% relative brightness. Image a) is DR, b) is SR, c) is Gaussian smoothing, and d) is deconvolution. Since the SR and Gaussian smoothing algorithms have more pixels, the horizontal scale was scaled to show identical relative size instead of simply number of pixels. All algorithms accurately maintained their relative irradiances. Note that the DR and Gaussian smoothing algorithms produced nearly identical results with the Gaussian smoothing algorithm providing smoother results. The SR and deconvolution algorithms produced the smallest FWHM curves showing that they have the best spatial resolution.

For completeness, the data from Figure 17 were run again for 545 nm point sources and displayed in Figure 18 to show the difference in performance when far from design. At 255 nm from the design wavelength of the FZP, all four algorithms are still able to maintain the relative brightness of the grayscale point sources. The DR, SR, and Gaussian smoothing algorithms have all spread out drastically becoming much less point-like and the SR algorithm no longer looks the best. The width of the deconvolution curve remains unchanged from Figure 17 indicating that it still appears as a point source despite being 255 nm from the design wavelength.

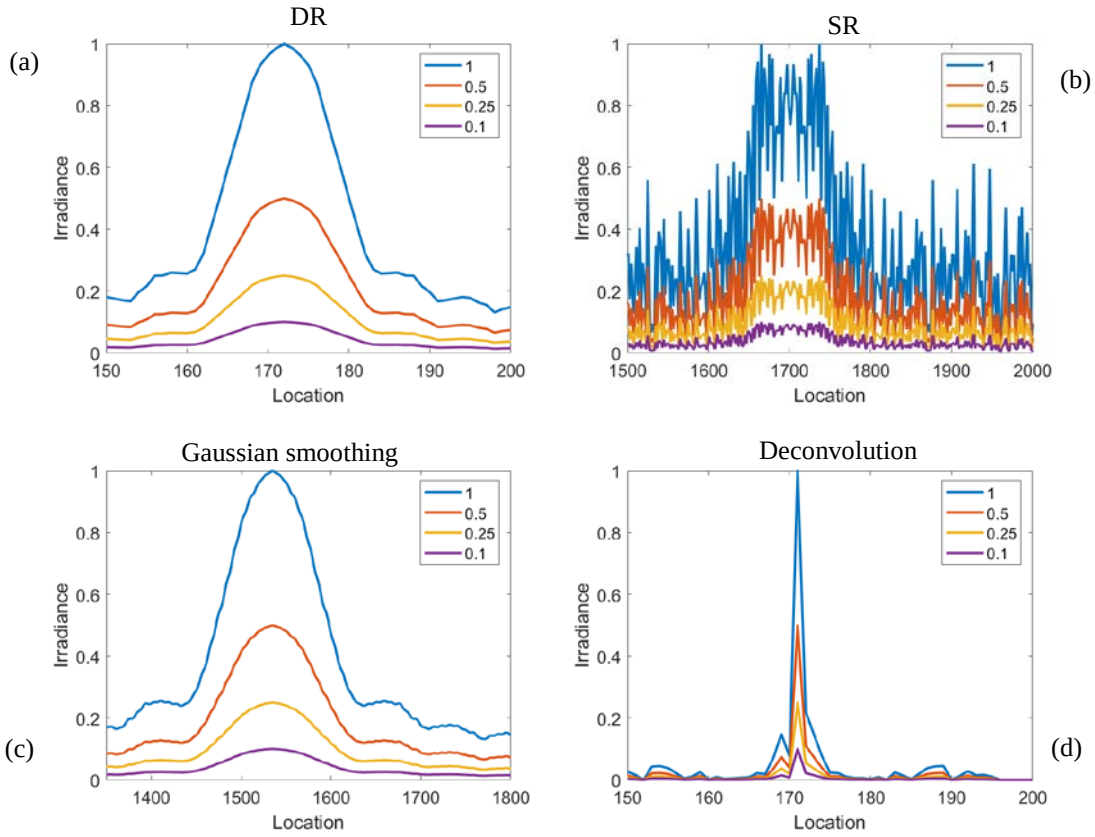

Figure 18. The relative irradiance by location on the refocused image detected from a simulated point source at 545 nm point sources that with 10%, 25%, 50%, and 100% relative brightness. Image a) is DR, b) is SR, c) is Gaussian smoothing, and d) is deconvolution. Since the SR and Gaussian smoothing algorithms have more pixels, the horizontal scale was scaled to show identical relative size instead of simply number of pixels. All algorithms accurately maintained their relative irradiances.

Finally, we look at a more complicated image with varying brightness levels at each location. All algorithms were able to handle the grayscale imaging well at 795 nm as shown in Figure 19. This close to the design wavelength, all algorithms performed similarly as they were all within the "perfect" range from Equation (10), we would expect similar performance from all of them. In order to better show the detail and difference, a zoomed in view of the first "S" in "STATES" is shown in Figure 20. Here, we see the Gaussian smoothing and SR algorithms producing better images. This is partially due to the increased pixel count that these methods provide. Additionally, another view of this pin was done while simulating it emitting at 400 nm in Figure 21. Here, we are a full 400 nm from the design wavelength of the FZP and so the DR, SR, and Gaussian smoothing algorithms are all unusable with the pin barely recognizable. The deconvolution algorithm run with 400 iterations, however, is able to produce results comparable to the results we got near design in Figure 19.

Figure 19. A more complicated image of an Air Force pin with various levels of brightness simulated to emit at 795 nm. Image is refocused using a) DR, b) SR, c) Gaussian smoothing, and d) deconvolution algorithms. All algorithms are able to accurately refocus the image near the design wavelength and since this is in the range of perfect refocusing, the algorithms all produce similar results.

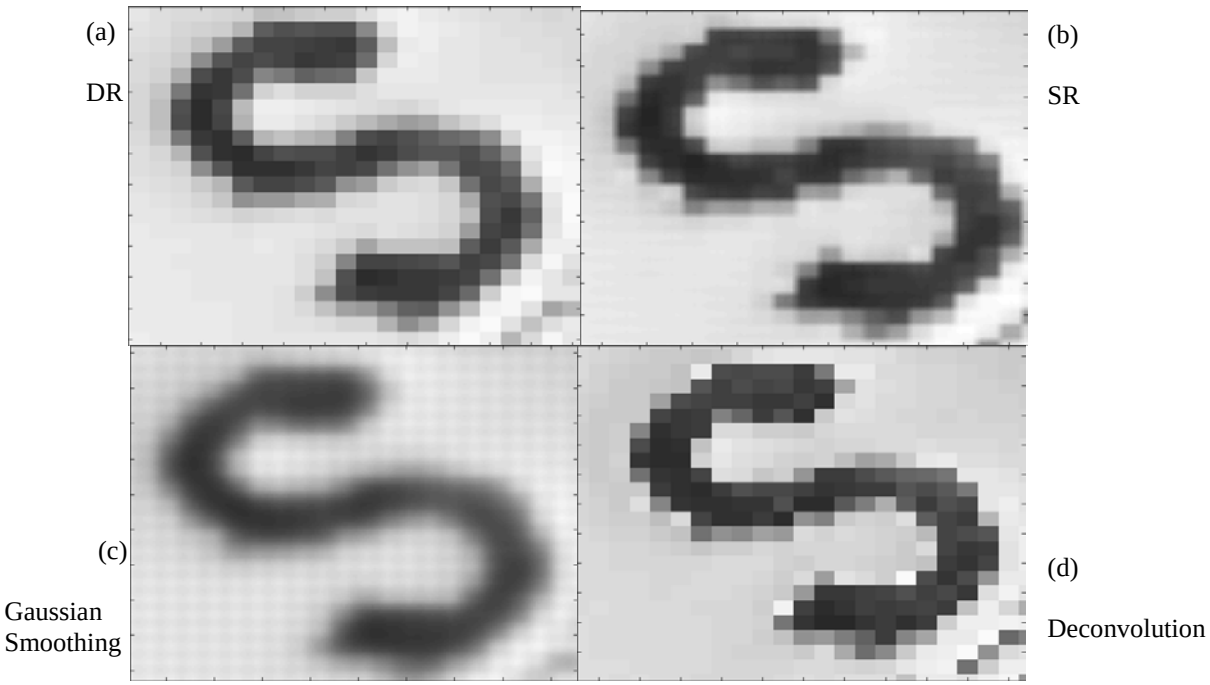

Figure 20. A more complicated image of an Air Force pin with various levels of brightness simulated to emit at 795 nm zoomed in on the first "S" in "STATES." Image is refocused using a) DR, b) SR, c) Gaussian smoothing, and d) deconvolution algorithms. In this zoomed in image, you can see the small differences between the different algorithms. Note that near design, for this image, the Gaussian smoothing and SR algorithms produce the best results.

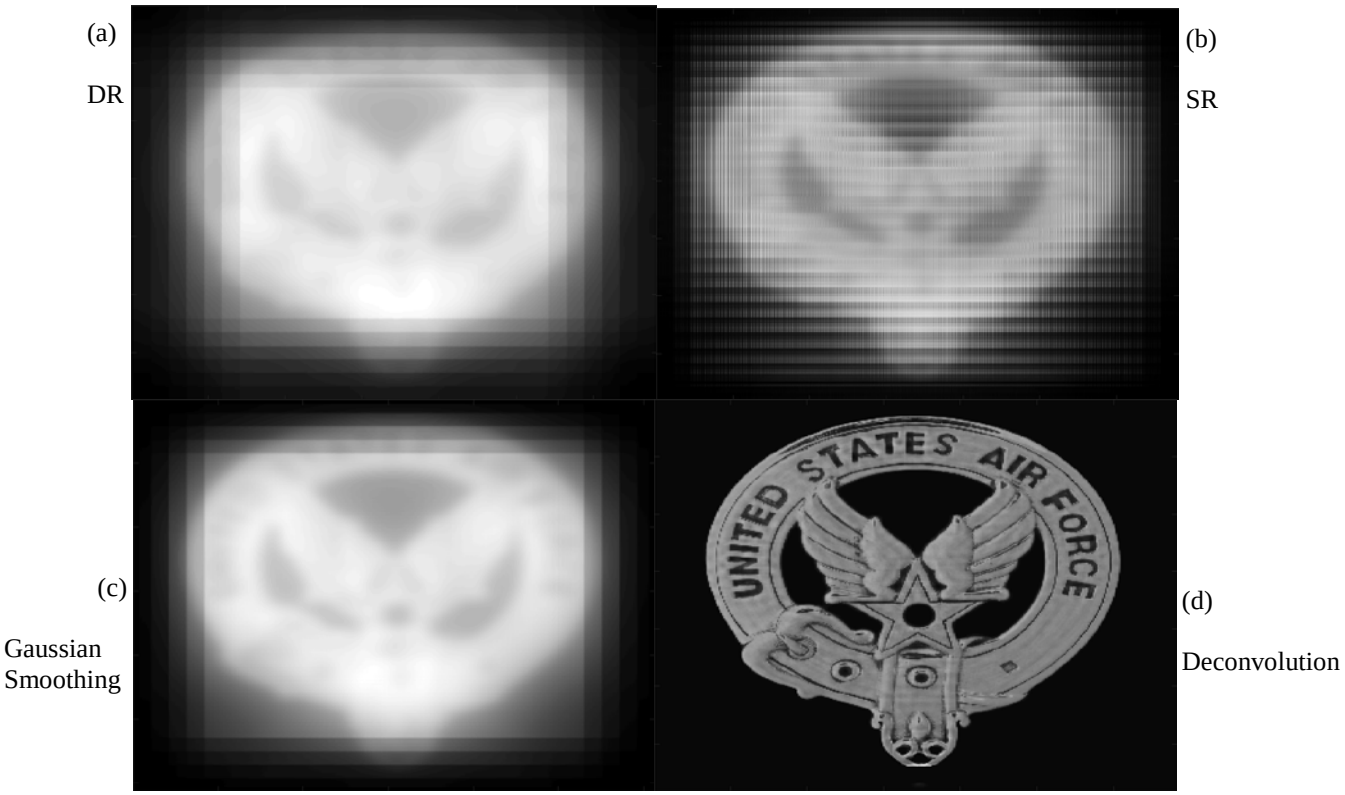

Figure 21. A more complicated image of an Air Force pin with various levels of brightness simulated to emit at 400 nm. Image is refocused using a) DR, b) SR, c) Gaussian smoothing, and d) 400 iteration deconvolution algorithms. When far from design, the DR, SR, and Gaussian smoothing algorithms are unable to refocus the image well while the deconvolution algorithm is.

Hyperspectral

Next, we will look at the hyperspectral performance of the algorithms. In order to do that, we will look at a generated image with the letters "SPIE" each emitting at a different wavelength as shown in Figure 22. The letters are emitting at 795 nm, 700 nm, 600 nm, and 500 nm respectively. Then we will look at the results when the same image is emitting at two different wavelengths. For this, we will use the USAF target.

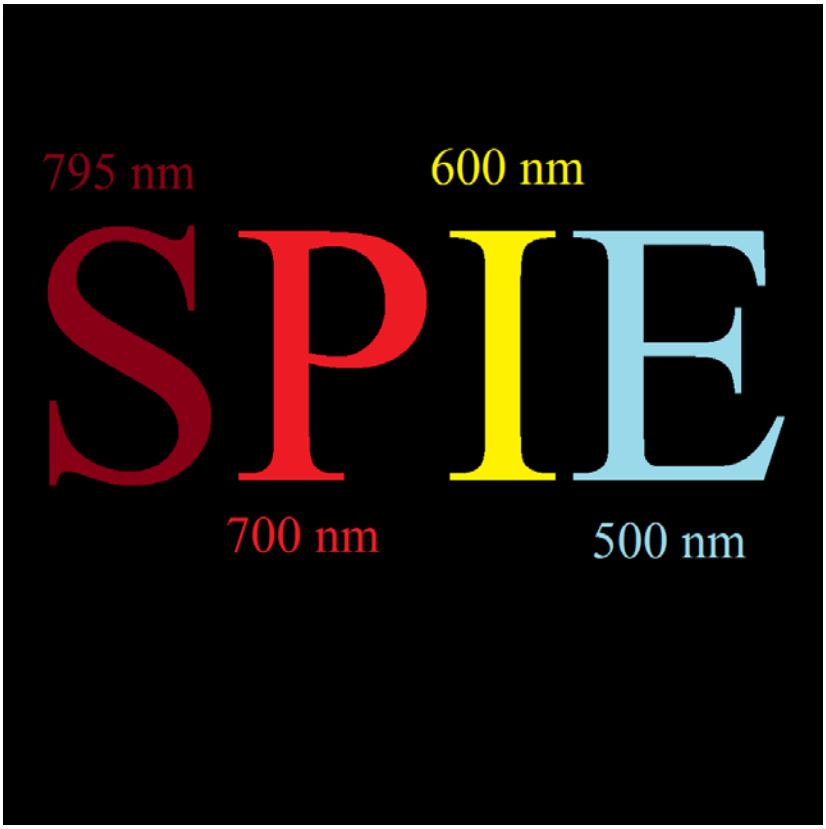

Figure 22. Simulated hyperspectral image. Each letter is output at a different wavelength as labeled in the image.

The image in Figure 22 was used to test the hyperspectral performance of each of the algorithms. Each algorithm was run on the image captured from the simulated hyperspectral "SPIE" and then refocused at 795 nm, 700 nm, 600 nm, and 500 nm. The results for DR are shown in Figure 23, the results for SR are shown in Figure 24, the results for Gaussian smoothing are shown in Figure 25, and the results for deconvolution are shown in Figure 26. The DR, SR, and Gaussian smoothing algorithms all work very well refocusing the "S" since that is near design. It is clear which letter we are focusing on and the rest of the letters are blurred into the background. As we move farther from the design wavelength, however, the ability to distinguish which letter is being focused

becomes more difficult. For all three of the algorithms, when we refocus at 500 nm, the only reason you can tell that that corresponds to the "E" is because we can compare it directly to 600 nm refocusing right next to it and see that the "I" has become slightly less focused. There are a few other features between these three algorithms that merit mentioning. First, as mentioned earlier, as we move farther from design, some of the image moves out of the micro-lens images due to the larger incident angle. This can be seen by the stair step feature on the edge of the 500 nm and 600 nm refocused image for the DR algorithm. The Gaussian smoothing algorithm also suffers from this, however, since we only use the center sub-aperture images that experience a smaller angle of incidence, this effect is minimized. Otherwise, the DR and Gaussian smoothing algorithm produced very similar results. Since the SR algorithm does not average out pixels like the DR algorithm does, every pixel is still there. Therefore, when we refocus on a wavelength that is not the wavelength that the image was emitting at, all the pixels are still there, just in the wrong place. We can see this from the hashing and pixilation of the other letters instead of the blurring seen in the DR and Gaussian smoothing algorithms. Finally, the deconvolution algorithm produced vastly different results. When refocused at different wavelengths, the deconvolution algorithm is able to minimize the irradiance of the other sources the best, however, there are still a few pixels that are still displayed. This is what causes the streaking in the images with deconvolution versus the blurring we see in the DR algorithm. Noise free, the best case was 400 iterations so that is what was shown. This matches the results we saw in Figure 8.

Figure 23. Hyperspectral image refocused with the DR algorithm at a) 795 nm, b) 700 nm, c) 600 nm, and d) 500 nm. The image contrast was adjusted to keep the image brightness comparable between images. The DR algorithm is able to refocus very well near design to differentiate wavelengths, however, as we get farther from design, that ability to differentiate wavelengths well disappears.

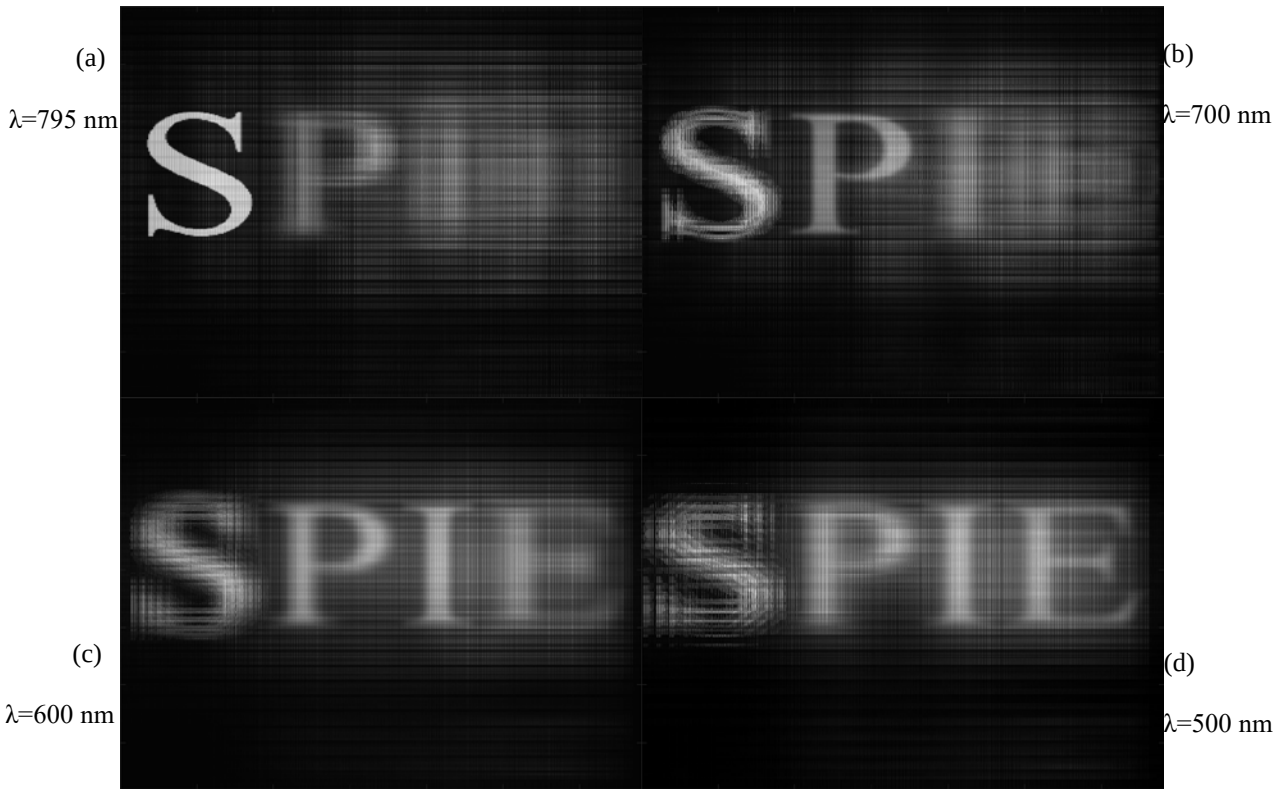

Figure 24. Hyperspectral image refocused with the SR algorithm at a) 795 nm, b) 700 nm, c) 600 nm, and d) 500 nm. The image contrast was adjusted to keep the image brightness comparable between images. The SR algorithm works well when near design to clearly demonstrate which wavelength is being measured, however, far from design, it is unable to clearly differentiate between wavelengths.

Figure 25. Hyperspectral image refocused with the Gaussian smoothing algorithm at a) 795 nm, b) 700 nm, c) 600 nm, and d) 500 nm. The image contrast was adjusted to keep the image brightness comparable between images. The Gaussian smoothing algorithm is able to refocus very well near design to differentiate wavelengths, however, as we get farther from design, that ability to differentiate wavelengths well disappears. This matches the results from DR.

Figure 26. Hyperspectral image refocused with the Deconvolution algorithm at a) 795 nm, b) 700 nm, c) 600 nm, and d) 500 nm. The image contrast was adjusted to keep the image brightness comparable between images. The deconvolution algorithm is able to separate the wavelengths near design and far from design. It does not completely get rid of the images that are recorded at wavelengths other than the wavelength being refocused at, but the image is blurry enough to imply that the algorithm should be rerun at other wavelengths to test for alternate source wavelengths.

If the spectral irradiance from single point from each of the letters in Figure 26 is examined, the reason for the other letters not disappearing completely becomes clear. This is shown in Figure 27. Notice that there is a large amount of cross-talk between the different wavelengths. This makes it seem as though they all have a peak near the design wavelength of 800 nm even though only the "S" is emitting near that wavelength. This is seen clearly in (a). The "S" is the only letter emitting near 800 nm, however, and it comes in much brighter than the other letters which is good. This still demonstrates a

limitation of the deconvolution algorithm when used near the design wavelength since the other letters should not show a peak there. In Figure 27 (b), the wavelengths above 725 nm are hidden so that the lower wavelengths can be seen. Here, the cross-talk is still evident by the noise present. However, the "P" has a peak at 700 nm, the "I" has a peak at 600 nm, and the "E" has a peak at 500 nm. These are all at the correct wavelengths that the letters were simulated to emit at. Therefore, while near the design there are still false peaks, the correct letter stands out above the rest. Additionally, farther from the design wavelength, the peaks from the sources line up correctly.

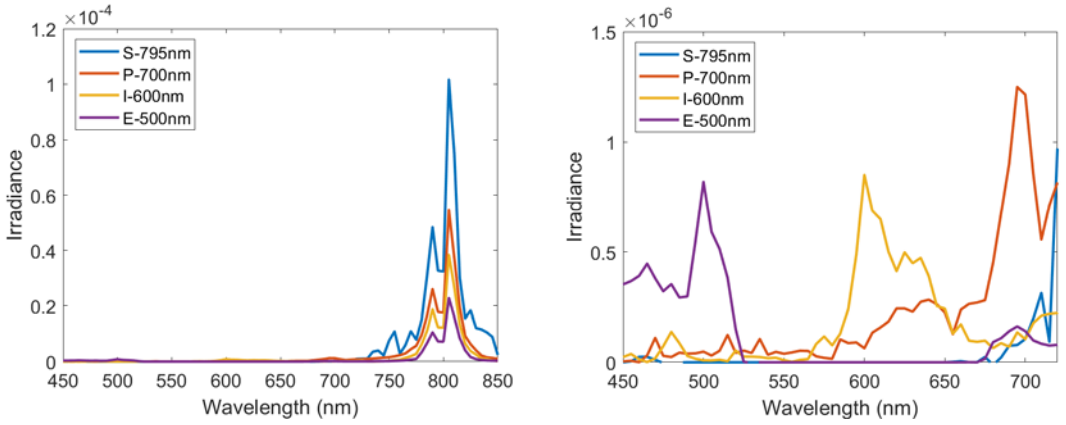

(a) (b)

Figure 27. The spectral irradiance curves from each of the letters from Figure 26 with (a) showing from 450 nm to 850 nm while (b) zooms in to better show the characteristics between 450 nm and 725 nm. The large amount of cross-talk causes a lot of noise in the image and false peaks near the design wavelength of 800 nm. However, farther from the design wavelengths, the measured spectral irradiance peaks line up correctly with the emitted wavelengths even though there is still noise from the cross-talk.

Finally, we looked at a hyperspectral USAF target. In this case, we had the USAF target from Figure 5 emitting at both 700 nm and 500 nm. The results when refocusing at 500 nm are shown in Figure 28 and the result when refocusing at 700 nm are shown in Figure 29. The deconvolution algorithm continues its trend of performing better farther from design with the image refocused at 500 nm looking the best out of all the images.

The DR and Gaussian smoothing images all have a very bright background due to the unfocused light from other wavelength spread out over the entire image. The same thing happens to the images refocused with the SR algorithm, except the unfocused light is not being averaged out over the entire scene. This leaves bright and dark pixel lines in the SR image corresponding to the incorrectly refocused pixels from the out of focus wavelength. While the deconvolution algorithm focused at 500 nm looks great, the one focused at 700 nm is much worse. This is due to the deconvolution algorithm confusing some of the 500 nm unfocused light for light displayed at 700 nm.

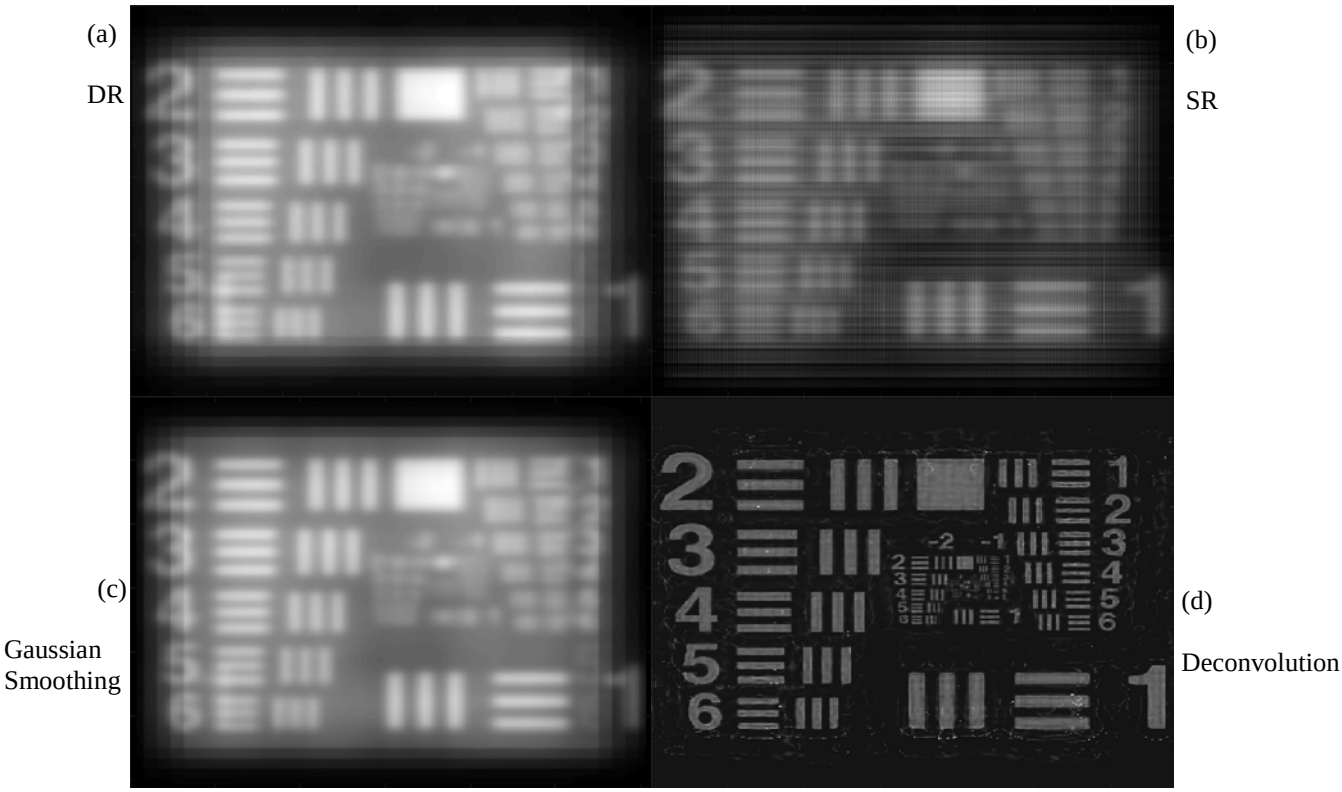

Figure 28. Hyperspectral USAF 1951 target emitting uniformly at 500 nm and 700 nm refocused at 500 nm using a) DR, b) SR, c) Gaussian smoothing, and d) 400 iteration deconvolution algorithms. Notice that DR, SR, and Gaussian smoothing algorithms are unable to refocus well as expected 300 nm from the design wavelength. However, deconvolution is still able to refocus with the same spatial resolution as a target emitting at a single wavelength, whether near or far from design, with the only side effect being a small amount of noise.

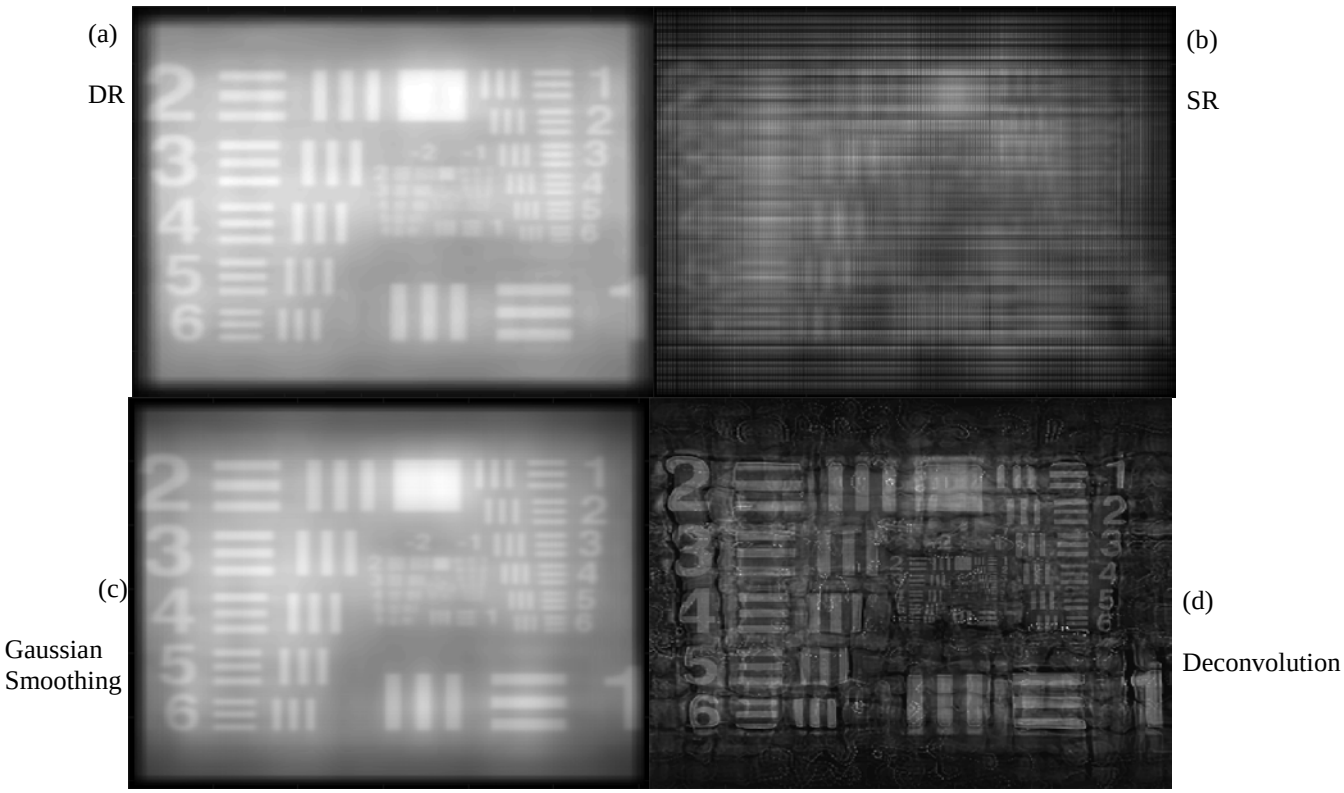

Figure 29. Hyperspectral USAF 1951 target emitting at 500 nm and 700 nm refocused at 700 nm using a) DR, b) SR, c) Gaussian smoothing, and d) 400 iteration deconvolution algorithms. The DR and Gaussian smoothing algorithms are able to produce results similar to what they got with a single wavelength 700 nm source with much more noise. The SR algorithm noise is too high to resolve the bars, however. Deconvolution is able to maintain the same resolution as before, however, the noise is much higher here since this is run closer to the design wavelength.

As an additional reference, Figure 30 shows the deconvolution algorithm even farther from design with the USAF target emitting at 475 nm and 495 nm. At these wavelengths, the other three algorithms are barely decipherable, however, the deconvolution algorithm is able to refocus the image to 475 nm at the same resolution that any of the algorithms were able to refocus when on design. There is a small amount of noise added due to the additional wavelength emitted and out of focus, but it is an otherwise clear and highly resolved image.

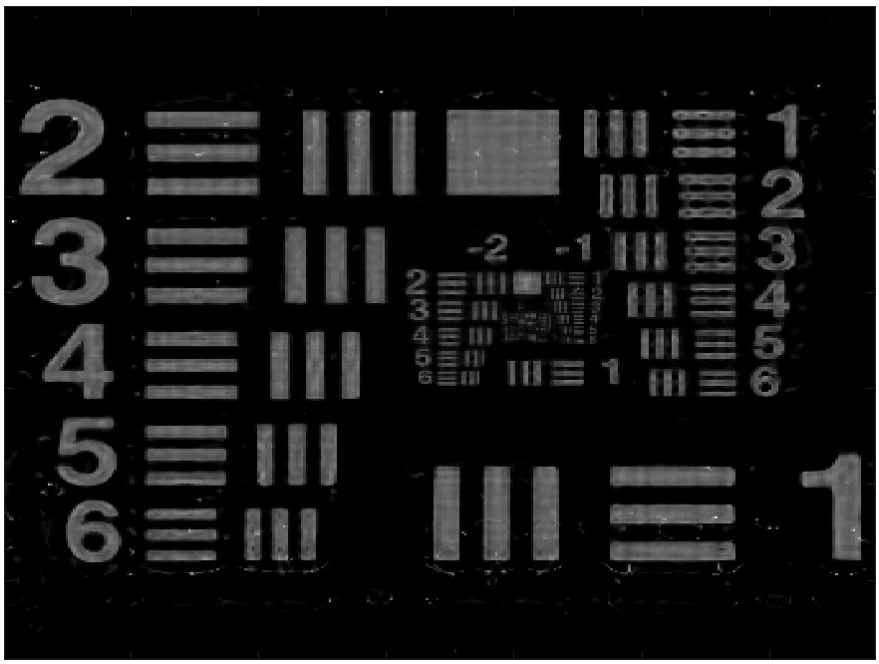

Figure 30. Hyperspectral USAF 1951 target emitting at 475 nm and 495 nm refocused at 475 nm using the deconvolution algorithm with 400 iterations. Now that we are 325 nm from the design wavelength, not only are we able to refocus fully on one of the wavelengths but the noise caused from the other wavelength is much smaller.

Performance and Analysis

Finally, with all the data collected, we determine the performance and characteristics of the different algorithms. This includes looking in the spatial domain to determine the spatial range and the spatial resolution. We also look into the spectral domain to find the spectral range and the spectral resolution of each of the algorithms. Finally, the required relative computation time for each of the algorithms is provided in case producing the results is time sensitive.

The spatial range is how wide of an area the diffractive plenoptic camera can view. Each pixel in the sub-aperture image views 0.01°. This gives us a total viewing range of 3.9°. Note that even though the SR and Gaussian smoothing algorithms have

more pixels in their final image, the sub-aperture images are limited to the same number of pixels as the DR and deconvolution algorithm so they all have the same spatial range.

Spatial resolution tells us the size of the smallest detectable separation between features. For this, we look at the IMD for various angular resolutions given from the USAF target in Figure 31. After comparing different images with various IMD values, an IMD of 0.03 was chosen as the value that would correspond to a particular bar grouping being resolved. Therefore, the best spatial resolution depends not only on the algorithm chosen, but also the wavelength. At 795 nm, 5 nm off design, all four algorithms were able to resolve down to 0.01°. This is the limit of our image as this represents the angular size of a pixel. As we move farther from design, the spatial resolution gets worse. By 750 nm, 50 nm off design, the DR, SR, and Gaussian smoothing algorithms along with deconvolution run with only 10 iterations are no longer limited by the pixel size. The only ones that maintained the same 0.01° resolution were the deconvolution algorithm run with 30 or more iterations. By the time we are 100 nm off design, only the deconvolution algorithm run with 100 or more iterations was able to maintain a 0.01° spatial resolution. At 500 nm, the DR, SR, and Gaussian smoothing algorithms are very poor with only able to resolve objects as small as 0.07°. Meanwhile, the deconvolution algorithm is able to keep the full 0.01° resolution, however, it requires 400 iterations in order to get this. At just 10 iterations, not even the largest bar grouping at 0.1° can be resolved. Another representation of this is given in Figure 7 which shows the smallest angular size able to be resolved on the USAF target given an IMD value of 0.03 is considered resolved.

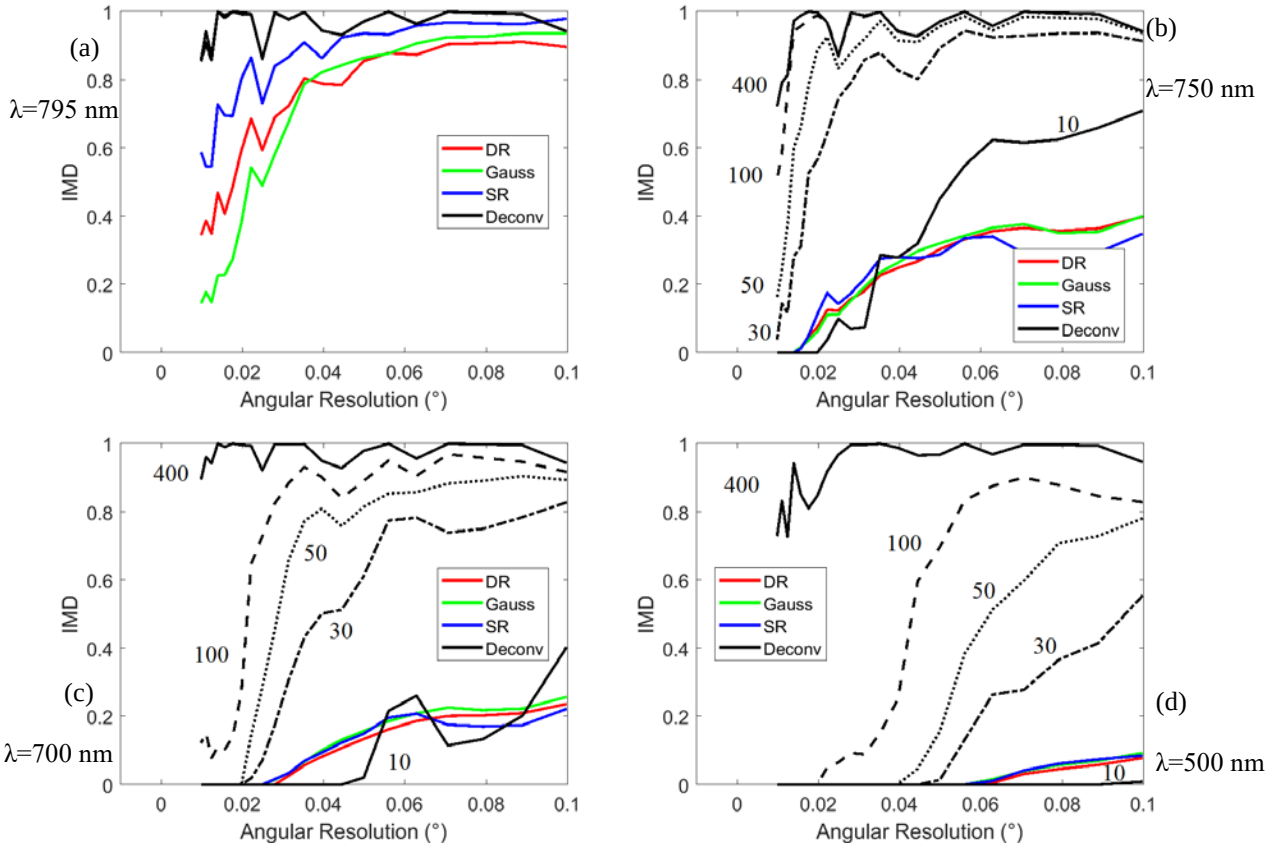

Figure 31. Calculation of the IMD when viewing the USAF target at different angular resolutions when the image is emitting and refocused at a) 795 nm, b) 750 nm, c) 700 nm, and d) 500 nm for DR, SR, Gaussian smoothing, and deconvolution. Deconvolution is run with 10, 30, 50, 100, and 400 iterations. Notice that near the design wavelength of 800 nm, all the algorithms are able to resolve the same number of bar groupings on the chart and deconvolution run with as few as 10 iterations produces identical results to deconvolution run with 400 iterations. However, as the emitted wavelength moves away from the design wavelength, the smallest angular features are no longer able to be resolved by any of the algorithms except for deconvolution with more than 100 iterations.

In addition to the spatial characteristics, we also have spectral characteristics we care about. The spectral range is displayed in Figure 7. The spectral range is therefore dependent on what resolution is required, what wavelength is being examined, and which algorithm is utilized. Note that all algorithms maintain the perfect refocusing that is limited by the pixel size for the range given in Equation (10). This gives us a perfect spectral range, regardless of algorithm, as long as we are within 30 nm of the design wavelength of the FZP. If a spatial resolution of 0.01° is required up to 400 nm from

design, the only option is the deconvolution algorithm with 400 or more iterations. The other algorithms, DR, SR, and Gaussian smoothing, are able to provide a spectral range of 100 nm from design if only a 0.04° spatial resolution is required.

In order to look at some of the characteristics of the point source, we tested all algorithms and the FWHM was measured for the measured irradiance versus the wavelength difference from the point source's emitted wavelength using the results from Figure 16 . The results are shown in Table 1 with the three algorithms based on the DR algorithm shown on the left and the deconvolution algorithm shown on the right and a margin of error of ±5 nm. Note that both the Gaussian smoothing and SR methods are based on the DR algorithm so their spectral resolutions were the same and are combined into the same section of the chart for clarity. We found that the angular resolution for the DR based algorithms got worse as the wavelength of the point source got farther away from the design wavelength of our FZP reaching nearly 100 nm once we were more than 200 nm off of design. The deconvolution algorithm, however, performed better as the wavelength of the point source got farther off of design with the spectral resolution reaching as good as 5 nm when 255 nm off of the FZP design wavelength. Overall, the deconvolution algorithm performed better at all wavelengths, but the spectral resolution was similar to the DR based algorithms near design and much better off design.

Table 1. FWHM of the DR based algorithms and the deconvolution algorithm at a given wavelength.

Source Wavelength	**DR-based resolution**	**Deconvolution resolution**
795 nm	20 nm	12 nm
745 nm	25 nm	14 nm
695 nm	45 nm	9 nm
645 nm	75 nm	8 nm
595 nm	90 nm	7 nm
545 nm	80 nm	5 nm

Similarly, there is the spectral resolution for the algorithms. This represents the minimum wavelength separation required between two point sources for them to be able to be separated. In order to determine whether or not individual sources are separately resolvable, the Rayleigh criteria is used [30]. This requires that the minimum between the indivual peaks drop below 85% of the peak value. When only 15 nm from design, within the perfect refocusing range, the DR, SR, and Gaussian smoothing algorithms are able to separate two point sources that are only 10 nm apart. Going down to 760 nm, however, the separation has to increase to 20 nm for the point sources to be able to be distinguished from each other. It gets rapidly worse from there. The deconvolution algorithm, however, gets better as the wavelength gets farther from design. When within 50 nm of design, a greater than 20 nm wavelength difference is required for two point sources to be resolved, and then it still is unable to be resolved in some cases. When 150 nm from design, however, the deconvolution algorithm is able to resolve point sources that are only separated by as little as 3 nm and when 250 nm from design, the deconvolution algorithm can resolve point sources separated by less than 2 nm. This allows a very accurate determination of the wavelength of multiple point sources when using the deconvolution algorithm far from design.

Another way to look at this is a contour plot of the size and irradiance of a point source refocused at different wavelengths. The DR algorithm is shown in Figure 32, the Gaussian smoothing algorithm is shown in Figure 33, the SR algorithm is shown in Figure 34, and the deconvolution algorithm is shown in Figure 35. These plots show a little bit of both spectral and spatial resolution in a single plot for point sources emitting

at 795 nm, 745 nm, and 595 nm and shows how the refocused point source is changing and evolving when refocused to other wavelengths. For these plots, the y-axis is the 1-D pixel locations of the point source and represents the spatial resolution, and the x-axis is the wavelength the algorithm refocused the point source to and represents the spectral resolution, and the contour is the measured irradiance values of the point source at the specified pixel location when refocused to the specified wavelength. Figure 32 shows a point source that was emitted at 795 nm, 745 nm, or 595 nm. Notice that the point spread function has a small spread in the both the spectral (x-axis) and spatial (y-axis) dimensions. However, as the emitted wavelength gets farther away from the design wavelength, the resolution decreases (the point spread function spreads out) in both the spectral and spatial dimensions. The Gaussian smoothing algorithm is shown in Figure 33 and the results are nearly identical to the DR algorithm.

The SR algorithm is shown in Figure 34. Here, only one source wavelength is shown since, because of the way that the SR algorithm is run, it is not able to produce a nice point spread function like DR or Gaussian smoothing are. That is because DR, and to a lesser extent Gaussian smoothing, average out the pixels at a certain location from the sub-aperture images. This means that when it is refocused at the wrong wavelength, the bright pixel locations don't line up to the position they are supposed to and so instead of the bright pixels being averaged together, the bright pixels are averaged with the dim pixel and you are left with just noise. The SR algorithm does not get rid of the data that way. Instead, it simply moves the pixel to the exact location that it is supposed be and then interpolates between the pixels to get a more exact representation of the source. However, when it is refocused to the wrong wavelength, all the bright pixels are still

there since they are not averaged away. So what you see is those bright pixels being moved farther and farther apart as the refocused wavelength gets farther from the wavelength that the point source was emitting at. This makes it so determining an exact spectral location is difficult using this method, however, if refocused at many wavelengths, as in this figure, the lines converge on the correct wavelength.

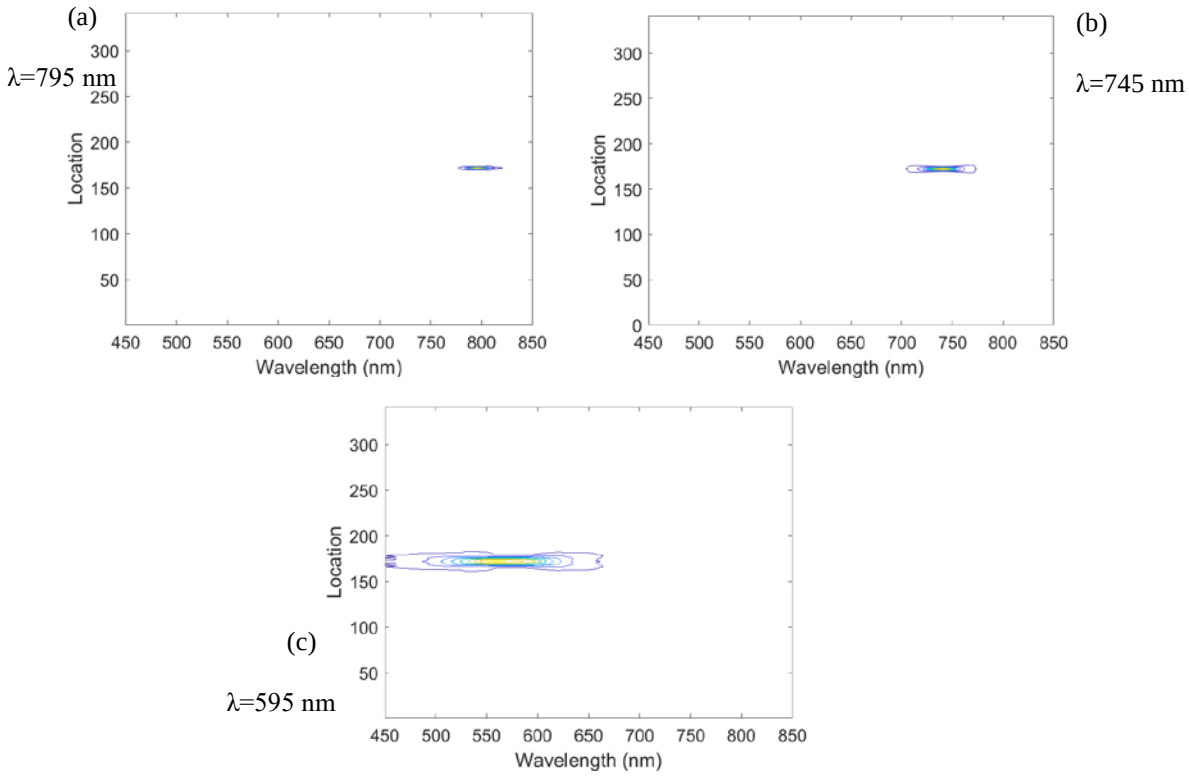

Figure 32. Point sources refocused using the DR algorithm, the x-axis is the wavelength refocused to, the y-axis is the 1-D pixel location of the point source, and the contour represents the relative irradiance calculated from the algorithm. The point source is emitting at a) 795 nm, b) 745 nm, and c) 595 nm. Note that the spectral resolution (x-axis) and the spatial resolution (y-axis) both get rapidly worse as the emitted wavelength gets farther from the design wavelength of 800 nm.

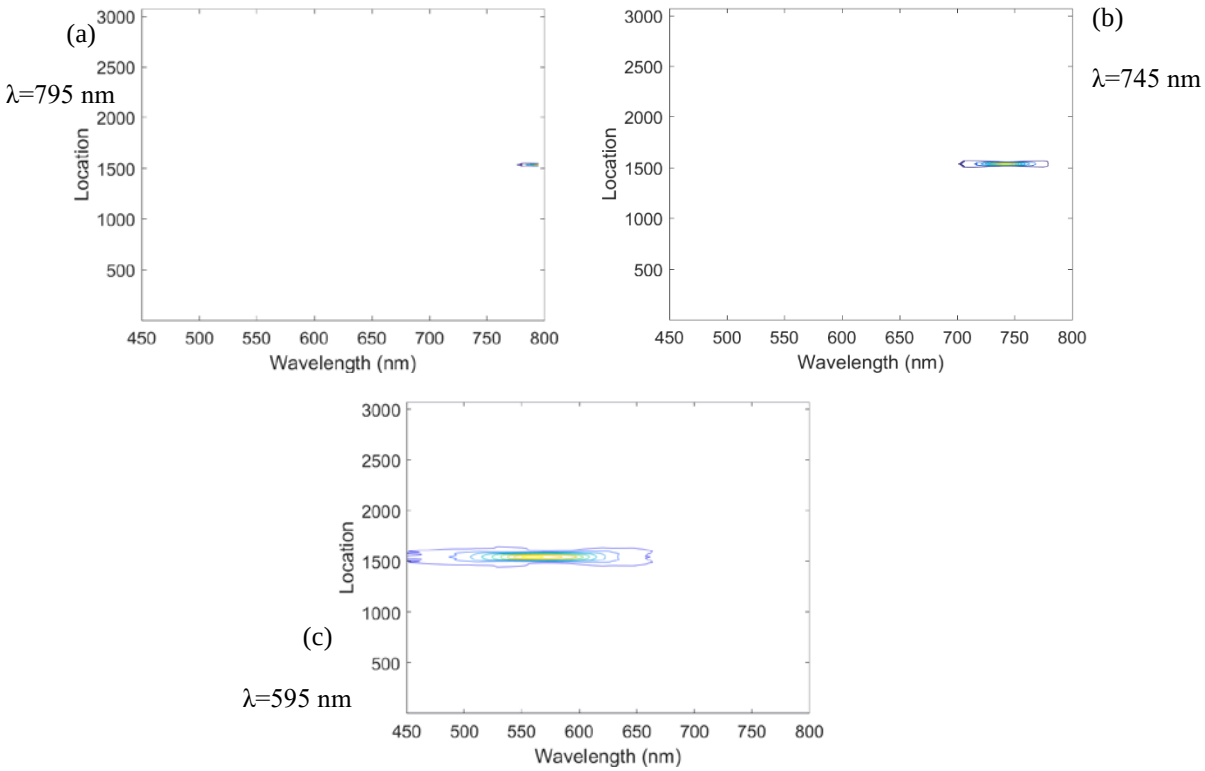

Figure 33. Point sources refocused using the Gaussian smoothing algorithm, the x-axis is the wavelength refocused to, the y-axis is the 1-D pixel location of the point source, and the contour represents the relative irradiance calculated from the algorithm. The point source is emitting at a) 795 nm, b) 745 nm, and c) 595 nm. Note that the spectral resolution (x-axis) and the spatial resolution (y-axis) both get rapidly worse as the emitted wavelength gets farther from the design wavelength of 800 nm.

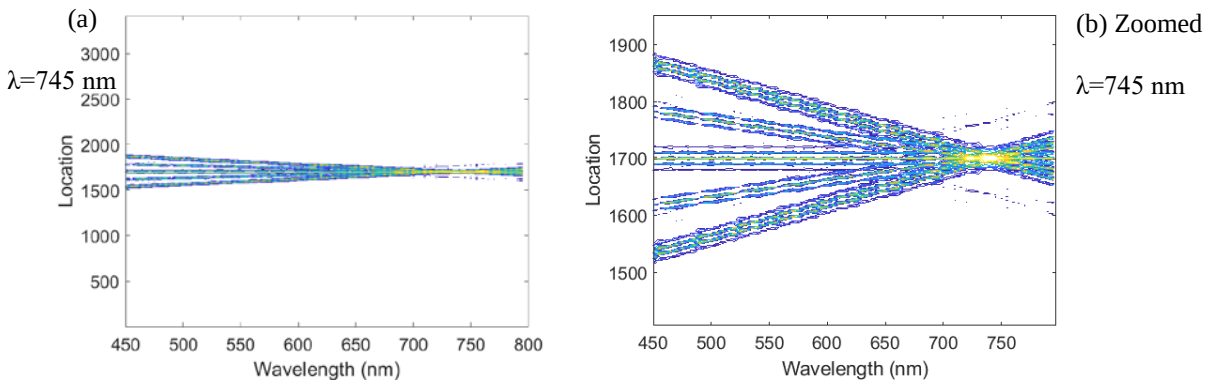

Figure 34. Point source refocused using the SR algorithm, the x-axis is the wavelength refocused to, the y-axis is the 1-D pixel location of the point source, and the contour represents the relative irradiance calculated from the algorithm. The point source is emitting at 745 nm and is shown at the same relative scale as the other figures in a) and zoomed in the spatial dimension, y-axis, in b). Note that we still get results recorded well outside the emitted wavelength so it is not directly comparable to DR, however, as the shifts due to the refocusing approach the correct wavelength, the points converge.

Finally, the deconvolution algorithm is shown in Figure 35. Notice that the size of the point spread functions is significantly smaller in both the spatial and spectral dimensions that the other algorithms; especially at 595 nm where we are more than 200 nm from the design wavelength. There are two very important features to take note of here. First, at 795 nm, near design, an extra point spread function appears. This can give a false positive and shows that some issues can arise when running the deconvolution algorithm near the design wavelength. Second, as the source wavelength gets farther from design, the point spread function gets tighter. This is the exact opposite of the results seen with the other algorithms. This reinforces the idea that the deconvolution algorithm performs better farther from design although it requires more iterations in order to get these results.

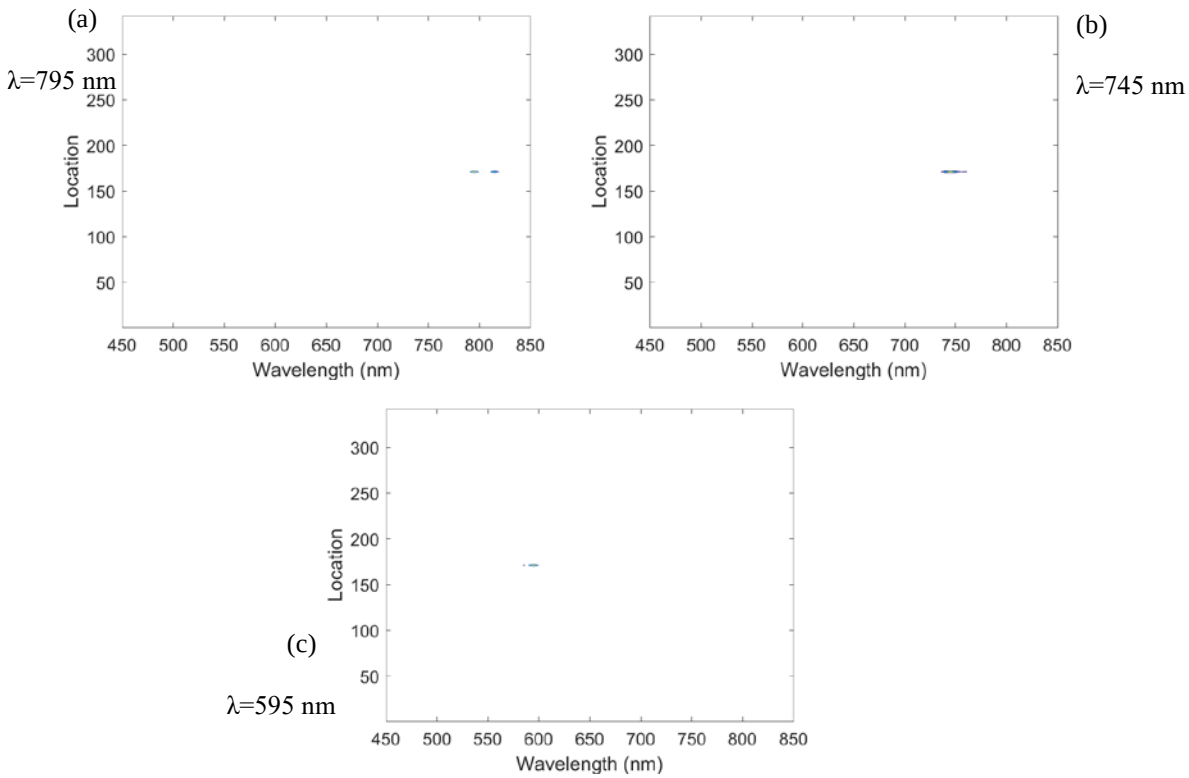

Figure 35. Point sources refocused using the deconvolution algorithm, the x-axis is the wavelength refocused to, the y-axis is the 1-D pixel location of the point source, and the contour represents the relative irradiance calculated from the algorithm. The point source is emitting at a) 795 nm, b) 745 nm, and c) 595 nm. Note that near the design wavelength of 800 nm, we get a false positive result near the actual wavelength. This can make it seem as though the point source is emitting at two different wavelengths. However, as we get farther from design, we not only don't get these false results anymore but the spatial and spectral spread is reduced giving better spatial and spectral resolution far from the design wavelength.

The final characteristic examined is the computation time. This is important because sometimes, the data is required within a certain time frame and unlimited computational time is not available. These calculations were run on an old AMD A4-5300B CPU running at 3.40 GHz. While these computation times won't compare directly to every computer, the relative computation time is what's most important and will provide the user with an easy reference for the relative time needed to perform each algorithm. The computation times are presented in Figure 36. The DR and SR algorithms both complete

a full run in 28 seconds with the SR algorithm being slightly faster. The Gaussian smoothing algorithm takes about 1.5 hours to complete a full run. The deconvolution algorithm scales linearly with the number of iterations performed with 400 iterations taking just over an hour.

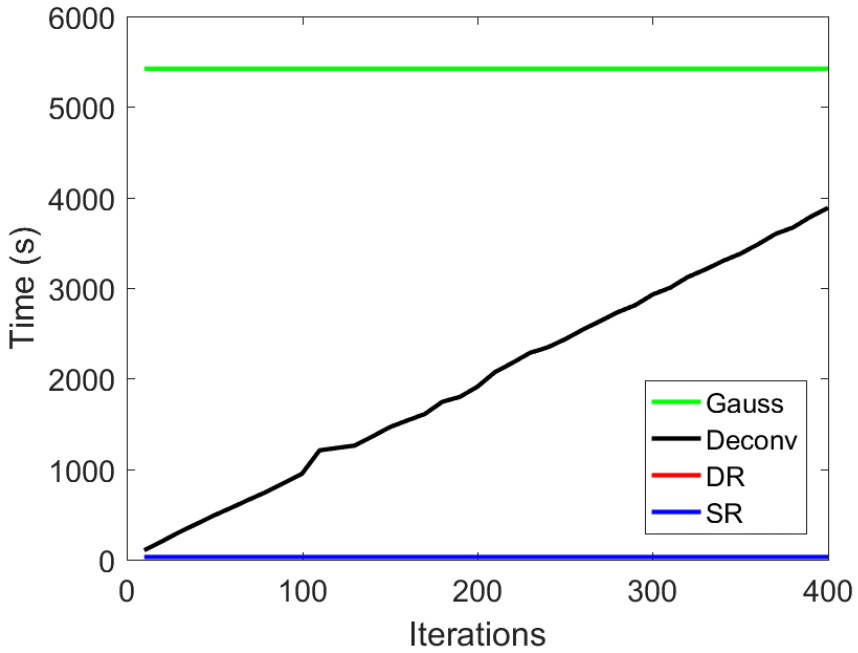

Figure 36. Computation time, in seconds, required for each of the four algorithms tested. DR, SR, and Gaussian smoothing don't have varying iterations, so they are displayed as a flat line while the deconvolution algorithm calculation time is determined based on the number of iterations performed.

V. Conclusions

The goal of this dissertation was to describe the analysis of the plenoptic camera with Fresnel zone plate imaging system to compare processing algorithm approaches for different desired capabilities. First, the results of a simulated single wavelength bar chart were analyzed with and without noise. Next, point sources were simulated in order to see how varying the wavelength separation from the FZP's design affected the efficacy of each algorithm. Then, grayscale and more complicated images were examined to determine if the algorithms were able to maintain the correct relative energies. Next, several hyperspectral cases were examined. Finally, the overall performance of the algorithms was examined.

To that end, each of the four algorithms provides results that exceed the others in certain situations, or when mission requirements dictate constraints upon the system. The Gaussian smoothing technique is better or equivalent to the digital refocusing technique in most cases, however, the difference is slight. The maximum angular resolution between the two is similar. Near design wavelengths, the DR provides sharp images and while the difference in the bar chart section of the chart is not as noticeable, the smoothing around the numbers does provide a noticeable improvement in image quality for the Gaussian smoothing algorithm over that of DR. Farther from the design wavelength, the DR algorithm is unable to completely focus the images so smoothing is not needed. The Gaussian smoothing algorithm does not generally worsen the results in this case, however, it does not significantly improve them either. Additionally, due to the shift that is required for the DR and Gaussian smoothing algorithms, the edge of the image can be lost on some of the sub-aperture images. After the sub-aperture images are

averaged together, this leaves a stair step effect on the edge of the final image since there are many blank edges being averaged into the final image. Since the Gaussian smoothing algorithm only uses the center sub-aperture images, this effect is reduced and so the Gaussian smoothing algorithm has better results near the edge of the image as the wavelength strays from design. Finally, the deconvolution algorithm is the most consistent. While it produced images on par or better than DR near design, the quality stayed consistent throughout the range of wavelengths studied provided that enough iterations were used. Near design, only a few iterations were needed to produce maximal quality images which took a few seconds and was on par with the time taken for the DR method. However, as the wavelength got farther away from the design wavelength of the FZP, more iterations were needed and the computation time increased.

If available computation time is a constraint, the DR algorithm provides broad quality available over a large wavelength range. However, if excess computation time is available and real-time results are not necessary, the Gaussian smoothing algorithm provided equivalent or better quality images in all cases than the DR algorithm while providing the best subjective quality for the numbers when near design. If the sample is primarily single wavelength near that of the design of the diffractive plenoptic camera, then the super resolution algorithm provided noticeably improved results. Since the improved quality rapidly degraded away from design, however, this method is only useful when able to work near the design wavelength. Finally, the Richardson-Lucy deconvolution algorithm performed comparable to the DR algorithm near the design wavelength while also performing nearly as well very far from design as near design. This allows single wavelength images to be recorded with near design quality, at nearly

any wavelength, with the same designed instrument, at the cost of only computation time. Noise can be an issue, however, it only affected the results for large numbers of iterations near design. This can be remedied by choosing a small number of iterations when near design, which is all that is needed and will also save on computation time, and only use more iterations when far from design. Additionally, deconvolution provided the best spectral resolution out of all of the algorithms. The spectral resolution improved for source wavelengths farther from design. With that in mind, if the computational power is available and the information does not need to be rendered real-time, the diffractive plenoptic camera can be designed so that the FZP design wavelength is outside of the wavelength range that is to be measured. This will require more iterations in order to reproduce the image, with corresponding increases in computational time, however, the spectral resolution can be maximized with this setup.

When viewing hyperspectral images, near design, the DR and Gaussian smoothing algorithms worked the best. Near design, these methods were able to identify different wavelengths with as little as 5 nm of spectral separation. When far from design, however, the DR, Gaussian smoothing and SR algorithms were very poor at separating multiple wavelengths in an image. The deconvolution algorithm, however, was able to produce incredible results and identify two separate wavelengths emitted by a single point source with less than 2 nm of spectral separations. With these qualifications in mind, the optimal algorithm can be chosen to provide the best results according to the time and wavelength constraints imposed upon the system.

Finally, when using a FZP, there is a tendency to try and design it so that the wavelengths that will be used will be as near the design wavelength as possible.

However, these results show that as long as you have the computation time available, the deconvolution algorithm works better when it is not near design. Therefore, if designing a diffractive plenoptic camera with the expectation to use deconvolution, the camera will work better if it is not designed to be centered at the wavelengths to be observed. Creating the FZP such that it is several hundred nanometers from the wavelengths being observed, while requiring more computational time, will minimize the dangers of noise, allow the smallest possible spectral resolution, and still maintain the spatial resolution that is possible near design.

Bibliography

[1] M. Swartwout, "The first one hundred CubeSats: A statistical look," *Journal of Small Satellites,* vol. 2, no. 2, pp. 213-233, 2013.

[2] A. Bürkle, F. Segor and M. Kollmann, "Towards autonomous micro uav swarms," *Journal of intelligent & robotic systems,* vol. 61, no. 1-4, pp. 339-353, 2011.

[3] M. Dearborn, G. Andersen and G. McHarg, "FalconSAT-7: A photon sieve solar telescope," *Air Force Academy, Colorado Springs, Co,* 2011.

[4] Z. Zhou and B. Xiangli, "Snapshot Multispectral Imaging Using a Plenoptic Camera with an Axial Dispersion Lens," *Computational Optical Sensing and Imaging,* pp. CTu2C-4, 2014.

[5] F. Hallada, "The Fresnel Zone Light Field Spectral Imager," *Air Force Institute Of Technology Wright-Patterson AFB OH Graduate School Of Engineering And Management,* 2017.

[6] J. A. Shepherd and A. L. Franz, "Evaluation of plenoptic algorithm performance for measuring scene spectra captured by a diffractive plenoptic camera," *Proc. SPIE 10669, Computational Imaging III,* p. 1066909, 2018.

[7] R. Ng, "Digital Light Field Photography," *Ph.D. dissertation, Standford University,* 2006.

[8] M. Broxton, L. Grosenick and S. Yang, "Wave optics theory and 3-d deconvolution for the light field microscope," *Opt. Express,* vol. 21, no. 21, pp. 25418-25439, 2013.

[9] T. E. Bishop and P. Favaro, "The Light Field Camera: Extended Depth of Field, Aliasing, and Superresolution," *IEEE Transactions on Pattern Analysis and Machine Intelligence,* vol. 34, no. 5, pp. 972-986, 2012.

[10] T. E. Bishop, S. Zanetti and P. Favaro, "Light field superresolution," *2009 IEEE International Conference on Computational Photography*, pp. 1-9, 2009.

[11] R. Ng, M. Levoy, M. Bredif, G. Duval, M. Horowitz and P. Hanrahan, "Light field photography with a hand-held plenoptic camera," *Computer Science Technical Report CSTR*, vol. 2, no. 11, pp. 1-11, 2005.

[12] G. Lippmann, "Epreuves reversibles donnant la sensation du relief," *J. Phys. Theor. Appl.*, vol. 7, no. 1, pp. 821-825, 1908.

[13] E. H. Adelson and J. R. Bergen, "The plenoptic function and the elements of early vision," *Vision and Modeling Group, Media Laboratory, Massachusetts Institute of Technology*, 1991.

[14] E. H. Adelson and J. Y. A. Wang, "Single lens stereo with a plenoptic," *IEEE Transactions on Pattern Analysis & Machine Intelligence*, vol. 2, pp. 99-106, 1992.

[15] R. A. Raynor, "Range Finding with a Plenoptic Camera," *Air Force Institute Of Technology Wright-Patterson AFB OH Graduate School Of Engineering And Management*, 2014.

[16] O. E. Meyers, "Studies of transmission zone plates," *Am. J. Phys.*, vol. 19, no. 6, pp. 359-365, 1951.

[17] E. Hecht, "Optics - 4th ed," *Addison Wesley*, 2002.

[18] M. Sussman, "Elementary Diffraction Theory of Zone Plates," *Am. J. Phys.*, vol. 28, no. 4, pp. 394-398, 1960.

[19] M. Young, "Zone plates and their aberrations," *J. Opt. Soc. Am.*, vol. 62, no. 8, pp. 972-976, 1972.

[20] Y. Park, L. Koch, K. D. Song, S. Park, G. King and S. Choi, "Miniaturization of a Fresnel Spectrometer," *J. Opt. A: Pure Appl. Opt.*, vol. 10, no. 9, p. 095301, 2008.

[21] F. Hallada, A. Franz and M. Hawks, "Fresnel zone plate light field spectral imaging," *Optical Engineering*, vol. 56, no. 8, 2017.

[22] F. D. Hallada, A. L. Franz and M. R. Hawks, "Fresnel zone plate light field spectral imaging simulation," *Proc. SPIE 10198, Algorithms and Technologies for Multispectral, Hyperspectral, and Ultraspectral Imagery*, p. 1019804, 2017.

[23] R. Ng, "Fourier slice photography," *ACM transactions on graphics (TOG)*, vol. 24, no. 3, pp. 735-744, 2005.

[24] S. C. Park, M. K. Park and M. G. Kang, "Super-resolution image reconstruction: a technical overview," *IEEE signal processing magazine*, vol. 20, no. 3, pp. 21-36, 2003.

[25] W. T. Freeman, T. R. Jones and E. C. Pasztor, "Example-based super-resolution," *IEEE Computer graphics and Applications*, vol. 22, no. 2, pp. 56-65, 2002.

[26] T. Georgiev, "Plenoptic camera resolution," *Applied Industrial Optics: Spectroscopy, Imaging and Metrology*, vol. JTh4A, no. 2, 2015.

[27] H. Zhang, "3D Surface Reconstruction Based On Plenoptic Image," *Ph.D. Thesis, Auburn University*, 2015.

[28] L. B. Lucy, "An iterative technique for the rectification of observed distributions," *Astronomical Journal*, vol. 79, no. 6, pp. 745-754, 1974.

[29] G. Boreman and S. Yang, "Modulation Transfer Function Measurement Using Three- and Four-bar Targets," *Appl. Opt.*, vol. 34, pp. 8050-8052, 1995.

[30] P. F. Meilan and M. Garavaglia, " Rayleigh Resolution Criterion for Light Sources of Different Spectral Composition," *Brazilian Journal of Physics*, vol. 27, no. 4, pp. 638-643, 1997.

[31] A. Lumsdaine and T. Georgiev, "The Focused Plenoptic Camera," *Computational Photography (ICCP), 2009 IEEE International Conference on. IEEE*, pp. 1-8, 2009.

[32] P. M. Lillo, M. L. Greene and V. Sick, "Plenoptic Single-Shot 3D Imaging of In-Cylinder Fuel Spray Geometry," *Zeitschrift fur Physikalische Chemie*, vol. 229, no. 4, pp. 549-560, 2015.

[33] P. Hartmann, I. Donko and Z. Donko, "Single exposure three dimensional imaging of dusty plasma clusters," *Review of Scientific Instruments*, vol. 84, no. 2, 2013.

REPORT DOCUMENTATION PAGE

Form Approved
OMB No. 074-0188

1. REPORT DATE *(DD-MM-YYYY)*	2. REPORT TYPE	3. DATES COVERED *(From – To)*
13-09-2018	PhD Dissertation	September 2015–September 2018

TITLE AND SUBTITLE
Evaluation And Quantification Of Diffractive Plenoptic Camera Algorithm Performance

5a. CONTRACT NUMBER

5b. GRANT NUMBER

5c. PROGRAM ELEMENT NUMBER

6. AUTHOR(S)

Shepherd III, Jack A., Captain, USAF

5d. PROJECT NUMBER

5e. TASK NUMBER

5f. WORK UNIT NUMBER

7. PERFORMING ORGANIZATION NAMES(S) AND ADDRESS(S)
Air Force Institute of Technology
Graduate School of Engineering and Management (AFIT/ENY)
2950 Hobson Way, Building 640
WPAFB OH 45433-8865

8. PERFORMING ORGANIZATION REPORT NUMBER
AFIT-ENP-DS-18-S-026

9. SPONSORING/MONITORING AGENCY NAME(S) AND ADDRESS(ES)
Intentionally left blank

10. SPONSOR/MONITOR'S ACRONYM(S)

11. SPONSOR/MONITOR'S REPORT NUMBER(S)

12. DISTRIBUTION/AVAILABILITY STATEMENT
DISTRUBTION STATEMENT A. APPROVED FOR PUBLIC RELEASE; DISTRIBUTION UNLIMITED.

13. SUPPLEMENTARY NOTES
This material is declared a work of the U.S. Government and is not subject to copyright protection in the United States.

14. ABSTRACT
A diffractive plenoptic camera is a novel approach to the traditional plenoptic camera which replaces the main optic with a Fresnel zone plate making the camera sensitive to wavelength instead of range. However, algorithms are necessary to reconstruct the image produced by plenoptic cameras. While many algorithms exist for traditional plenoptic cameras, their ability to create spectral images in a diffractive plenoptic camera is unknown. This paper evaluates digital refocusing, super resolution, and 3D deconvolution through a Richardson-Lucy algorithm as well as a new Gaussian smoothing algorithm. All of the algorithms worked well near the Fresnel zone plate design wavelength, but Gaussian smoothing provided better looking images at a cost of high computation time. For wavelengths off the design wavelength, 3D deconvolution produced the best images but also required more computation time. 3D deconvolution also had the best spectral resolution, which increased away from the design wavelength. These results, along with consideration of mission constraints and spectral content in the scene, can guide algorithm selection for future sensor designs.

15. SUBJECT TERMS
plenoptic camera, image processing, diffractive plenoptic camera

16. SECURITY CLASSIFICATION OF:			17. LIMITATION OF ABSTRACT	18. NUMBER OF PAGES	19a. NAME OF RESPONSIBLE PERSON
a. REPORT	b. ABSTRACT	c. THIS PAGE			Lt Col Anthony Franz, AFIT/ENP
U	U	U	UU	92	19b. TELEPHONE NUMBER *(Include area code)* (937) 255-6565, ext 4429 (Anthony.Franz@afit.edu)

Standard Form 298 (Rev. 8-98)
Prescribed by ANSI Std. Z39-18